AIMS Geosciences

AIMS Geosciences, 12(1): 96–126.
DOI: 10.3934/geosci.2026004
Received: 19 February 2025
Revised: 01 December 2025
Accepted: 05 January 2026
Published: 20 January 2026

https://www.aimspress.com/journal/geosciences

Research article

Characterisation of the Kilmuckridge geotechnical test site

Sathwik S Kasyap[1], Kevin N Flynn[1], MB Mohammed[1], J Labergere[1,2] and David Igoe[1,*]

[1] Department of Civil Structural and Environmental Engineering, Trinity College Dublin, Dublin 02, Ireland
[2] Grenoble INP - Ense3, Université Grenoble Alpes, France

* **Correspondence:** Email: igoed@tcd.ie; Tel: +353 1 896 1112.

Abstract: The paper describes the characterisation of a test site in an active sand quarry located near Kilmuckridge, County Wexford, Ireland. Two test areas have been selected in this 47-acre sand and gravel quarry, approximately 150 m apart. Test Area A covers an area of approximately 3100 m^2, and Area B is approximately 1500 m^2. Both test areas are over-consolidated with dense to very dense deposits; Area A has slightly gravelly sand to silty sand layers, and Area B is primarily sandy silt. A series of pile lateral and axial load tests are planned at the two sites. In Area A, CPT cone tip resistance q_c values up to 60 MPa were recorded in the top 2 m, with the values dropping to approximately 20 MPa in deeper layers below 2 m. The paper presents the results from in situ cone penetration tests, geotechnical laboratory characterisation tests on disturbed samples, and chemical characterisation analyses. Shear box tests and drained monotonic triaxial tests were performed on reconstituted sand samples to investigate the shear strength.

Keywords: sand; silt; CPT; pile testing

1. Introduction

The design of offshore wind turbine (OWT) foundations demands a comprehensive understanding of soil-structure interaction, particularly under the complex cyclic and dynamic loading conditions

characteristic of the offshore environment. Geotechnical test sites offer an important platform for empirical validation of foundation performance, enabling the controlled observation and measurement of load responses under site-specific conditions [1,2]. These test sites facilitate the refinement of analytical and numerical models, which are essential for optimising design approaches and mitigating risk in offshore wind developments [3].

Site characterisation is a prerequisite for meaningful interpretation of testing data. Detailed knowledge of stratigraphy, soil composition, stress history, stiffness, and strength parameters allows for the calibration of design methodologies and enhances the reliability of extrapolating findings to full-scale applications [4,5]. Moreover, accurately characterised test beds support the development and validation of novel foundation systems, such as suction caissons and monopile extensions, which are increasingly relevant in deeper waters and more demanding seabed conditions [6]. In Ireland, the characterisation of the Blessington geotechnical test site [7], using both in situ and laboratory tests, has provided a basis for validating various lateral and axial pile designs for offshore applications [8,9].

Advancements in site investigation tools and methods have significantly enhanced the accuracy and efficiency of offshore geotechnical characterisation, directly supporting the development of reliable foundation design for offshore wind infrastructure. Cone penetration testing (CPT) systems, in-situ pressuremeters, full-flow penetrometers, and seismic CPT have been providing high-resolution profiling of soil stratigraphy and mechanical properties with minimal disturbance [10,11]. Additionally, integration of geophysical surveys with geotechnical data, through methods like multichannel seismic imaging and electrical resistivity tomography, has improved spatial continuity and reduced uncertainty in subsurface interpretation [12]. More recently, the ROBOCONE project, under the collaboration of the University of Bristol, the University of Southampton, and Trinity College Dublin, is developing a next-generation robotic tool to enhance ground characterisation for the whole-life design of infrastructure [13,14]. As the offshore wind sector expands, the strategic use of geotechnical test sites will remain central to reducing design conservatism, lowering construction costs, and ensuring the long-term performance of foundation infrastructure.

This paper discusses the characterisation of a geotechnical testing site, which will be used as a test bed for large-scale model pile load tests, as well as the testing and validation of the ROBOCONE tool and design methods. The test site is an active quarry for sand and gravel in Ballynamona, Co. Wexford (near Kilmuckridge Village), approximately 1 km from the east coast of Ireland. The authors identified this area as a potential geotechnical test site in 2023 for medium-scale (200–1000 mm diameter) axial and lateral pile testing, supporting various research projects at Trinity College Dublin. The Blessington Redbog quarry [7] was used for similar purposes until 2023. The primary reasons for the selection of this new test site in Kilmuckridge over Blessington are (i) the presence of a water table close to the surface (~1 m below ground level) and (ii) the lateral and vertical heterogeneity of soil deposits, unlike uniform sand in Blessington. The heterogeneity includes the presence of dense, slightly gravelly sand overlaying uniform silty sand in Area A and gravelly sand overlaying fine sandy silt in parts of Area B. These conditions of lateral and vertical heterogeneity provide an ideal opportunity to understand the behaviour of foundations in varied geological materials.

2. Test site and location

The test site is located within a sand pit quarry owned and operated by Roadstone Limited, located approximately 100 km south of Dublin (Figure 1a). The quarry is located in the townland of Ballynamona in Kilmuckridge, Co. Wexford, with the east coast of Ireland situated 1 km to the east. Two test areas, Area A and Area B, were identified away from the current activities in the quarry but closer to the access roads (Figure 1b). Both test areas were previously quarried (approximately 50 m of sand deposit), and no further quarrying activity is planned in these areas, primarily due to the close proximity of the groundwater table to the existing ground level. Keeping a reasonable offset from the peripheral hill toes (~10 m), Area A constitutes a ~3200 m^2 circular area, whereas Area B, ~150 m southeast of Area A, constitutes a ~1900 m^2 area. Figure 1c and Figure 1d show a closer view of Area A and Area B, respectively.

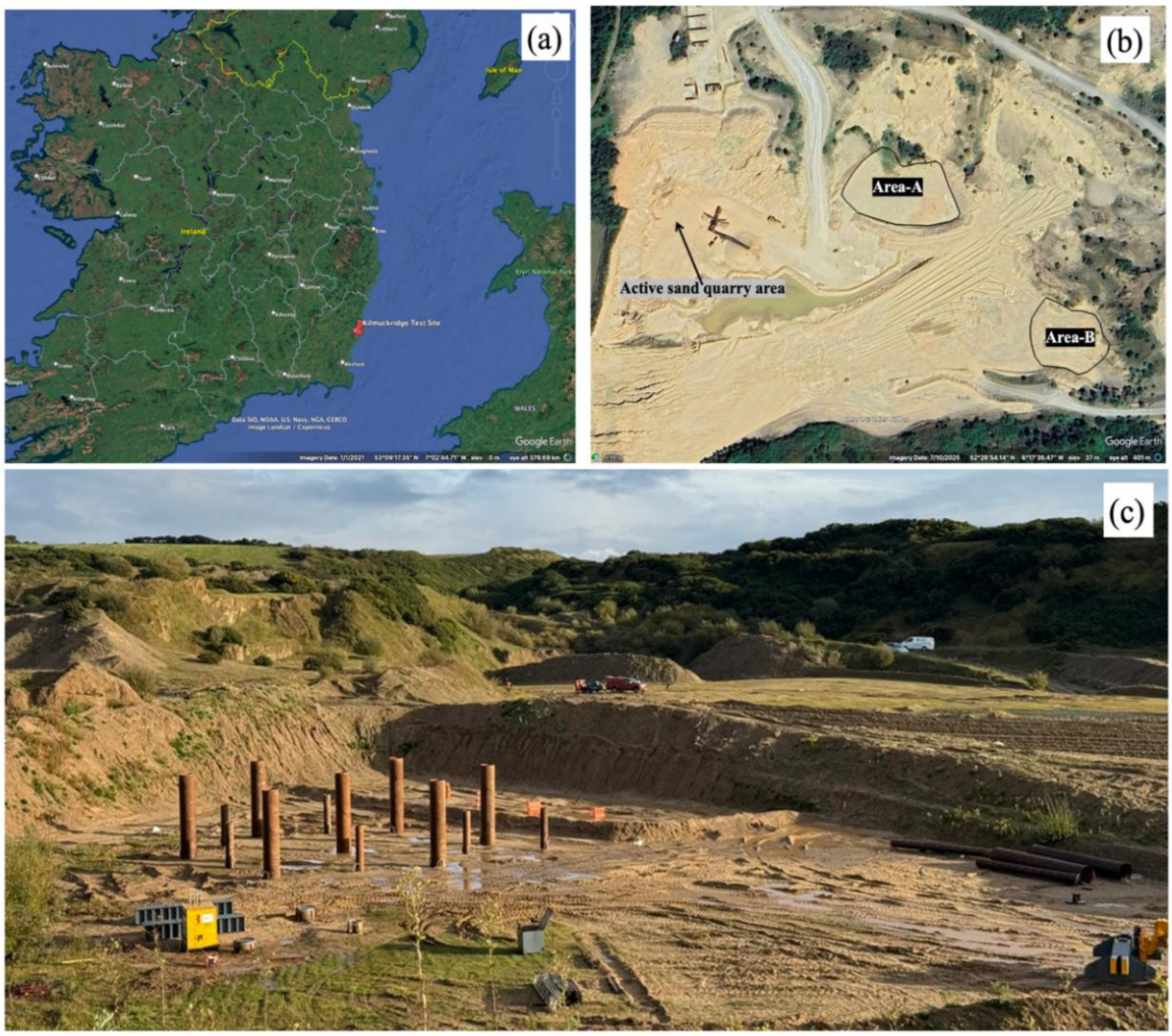

Figure 1. (a) Location of Kilmuckridge testing site. (b) Aerial view of Roadstone quarry showing test areas. (c) Elevated view of both areas A (foreground) and B (background).

3. Geological setting

3.1. Bedrock geology

The bedrock geology of the Kilmuckridge area consists of greywackes and slates from the Cambrian period [15]. Bedrock outcrops have been identified in Kilmuckridge village, approximately 2 km north of the test site. However, bedrock was not encountered within the relevant depths during the ground investigations described in Section 4. As such, the bedrock geology is not discussed further herein.

3.2. Quaternary geology

A comprehensive synopsis of the Quaternary geology of South Wexford is provided in [16]. The landscape within the Kilmuckridge region is dominated by a series of steeply sided glacial mounds of sand and gravel, known as kames, which were deposited during the melting and recession of ice sheets at the end of the last Ice Age [17].

The variable rates of deposition during the melting process have resulted in highly complex stratigraphic sequences within these kame deposits. The Geological Survey of Ireland's (GSI) Quaternary Drift Map series for the area, published in the late 1800s, reports fine sand and gravel at the surface of the present-day Kilmuckridge quarry, with exposed cliff faces along the coastline to the east, revealing alternating sequences of sand, gravel, and calcium-rich clays. The lithology of the gravel particles within these strata is also variable, with shale, quartz, granite, and flint frequently reported. Marine shells have also been identified on occasion.

Historical topography maps published by Ordnance Survey Ireland indicate a peak elevation of +73 m above the Irish Ordnance Datum (OD) at the test site. However, following the commencement of commercial quarrying operations at the site in the 1960s, the internal level within the quarry had been gradually reduced to its present-day elevation of approximately +20 mOD. Visual inspection of the exposed internal faces within the quarry confirms the findings reported by the GSI historical drift maps, which comprise alternating layers of coarse- and fine-grained material.

4. Characterisation techniques

A series of ground investigations has been commissioned by Trinity College Dublin at the site to characterise the ground and groundwater conditions in the two test areas (see Figure 2). These techniques comprised:

- 4 Nr cable percussion boreholes (BH1 to BH4) to depths between 7 and 10 m below ground level (bgl) to obtain samples for classification purposes.
- Cone penetration tests with pore pressure measurements (CPTu) to depths of 10–12 m bgl.
- 4 Nr seismic cone penetration tests (SCPT) to depths of 10–12 m bgl.
- 2 Nr standpipe piezometers for groundwater sample and monitoring in both test areas.
- 7 Nr of 1D and 2 Nr of 2D multi-channel analysis of surface waves (MASW) testing across the test areas.
- Geotechnical, microscopic, and chemical laboratory characterisation tests.

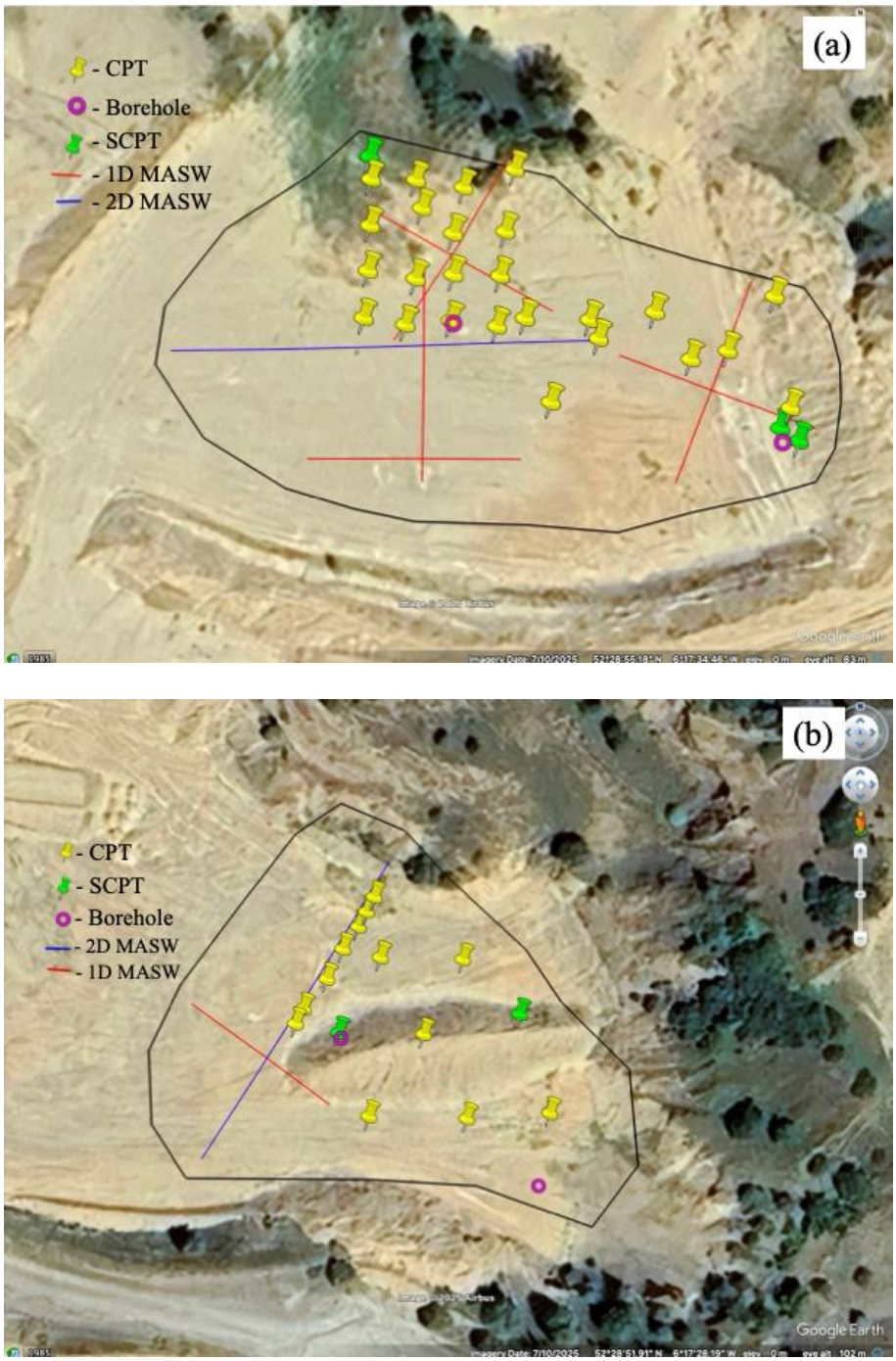

Figure 2. Location map of all in situ characterisation tests performed at Kilmuckridge (a) Area A and (b) Area B.

5. Groundwater

The groundwater regime at the site was investigated by installing standpipe piezometers in each test area. These installations comprised a 50 mm diameter uPVC pipe with a slotted section over a 1 m response zone containing pea gravel, which was sealed by 0.5 m thick bentonite seals. Further details are provided in Table 1.

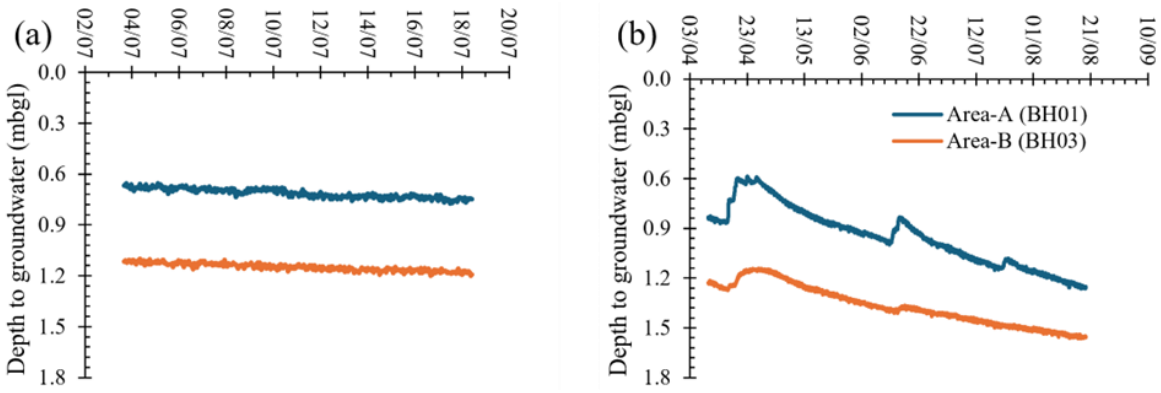

Figure 3. Variation in groundwater levels for (a) July 2024 and (b) April to August 2025.

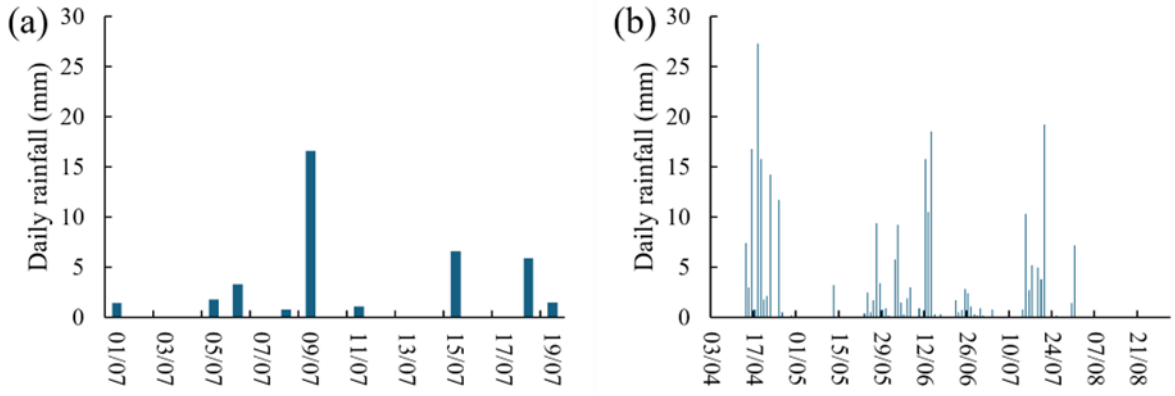

Figure 4. Rainfall records near the Kilmuckridge test site for (a) July 2024 and (b) April to August 2025.

Table 1. Details of standpipe piezometer installations.

Area	Borehole	Response zone (m bgl)	Stratum
A	BH1	2.5–3.5	Medium dense sand
B	BH3	2.0–3.0	Dense, slightly gravelly sand

Short-term groundwater monitoring was initially carried out over a two-week period in June 2024 at both test areas using automatic logging probes (compensated for variations in barometric pressure), with a further long-term monitoring period undertaken from April to August 2025 to assess seasonal variations in groundwater across the site. The results of the groundwater levels with time for the two areas are shown in Figure 3a and b. Groundwater levels range from 0.6 to 1.3 m bgl in Area A and from 1.1 to 1.6 m bgl in Area B. The long-term monitoring shows a gradual downward trend in groundwater level over the 4-month monitoring period, which is attributed to below-average rainfall levels during this time. The corresponding daily rainfall recorded at the nearest meteorological station located 25 km southeast of the site at Johnstown Castle, Co. Wexford, plotted for both monitoring periods in Figure 4, confirms this, with periods of prolonged rainfall leading to temporary increases in groundwater level.

6. Sample description

Disturbed samples were obtained from the four cable percussion boreholes in two test areas. Table 2 presents the depth of the samples collected from each borehole and provides a visual description of each sample. BH1 and BH2 in Area A and BH3 in Area B encountered predominantly gravelly sand to silty sand conditions, mostly golden brown (Figure 5a). In contrast, BH4 in Area B showed significant silt content, which is dark grey (Figure 5b). Visual observation of sand and gravel grains indicated subrounded to angular shape.

Table 2. Summary of ground investigation methods undertaken by TCD.

BH No.	Sample label	Depth (m)		Visual description	BH No.	Sample label	Depth (m)		Visual description
1	A	1.3	1.7	Slightly gravelly sand	3	A	0.8	1.0	Slightly silty sand
	B	2.4	2.7			B	1.2	1.5	
	C	2.7	3.0			C	1.7	2.0	
	D	3.4	3.7			D	2.2	2.5	
	E	4.3	4.6	Stiff sandy silt		E	2.7	3.0	
	F	5.4	5.7	Slightly silty sand		F	3.2	3.5	Slightly gravelly sand
	G	6.3	6.7	Silty sand		G	3.7	4.0	
	H	7.1	7.5			H	4.3	4.5	
2	A	0.8	1.2	Slightly gravelly sand		I	4.7	5.0	
	B	1.6	2.0			J	5.3	5.6	
	C	2.3	2.6			K	5.8	6.1	
	D	3.3	3.5			L	6.3	6.6	Gravelly sand
	E	3.8	4.0	Stiff sandy silt		M	6.8	7.2	
	F	4.2	4.5	Gravelly sand	4	A	1.0	1.5	Slightly gravelly sand
	G	5.2	5.5			B	1.8	2.4	
	H	5.7	6.0			C	2.5	3.0	Slightly sandy silt
	I	6.2	6.5			D	3.2	3.6	
	J	6.6	6.9			E	3.7	4.0	
	K	7.0	7.2	Silty sand		F	4.5	4.8	
	L	7.7	8.0			G	5.2	5.5	
	M	8.1	8.3			H	5.7	6.0	

Figure 5c–d shows the variation of natural moisture content with depth. In boreholes BH1, BH2, and BH4, at shallow depths, the natural moisture content increased with depth, but below the silt layer

(between 2.5 and 4 m depth), the natural moisture content became constant. This change in water content behaviour was also reflected in the pore water pressure variations (u_2) during cone penetration tests (discussed in Section 10). However, in BH3, where silty sand overlaid with gravelly sand was observed, the natural moisture content remained almost constant with slight variations.

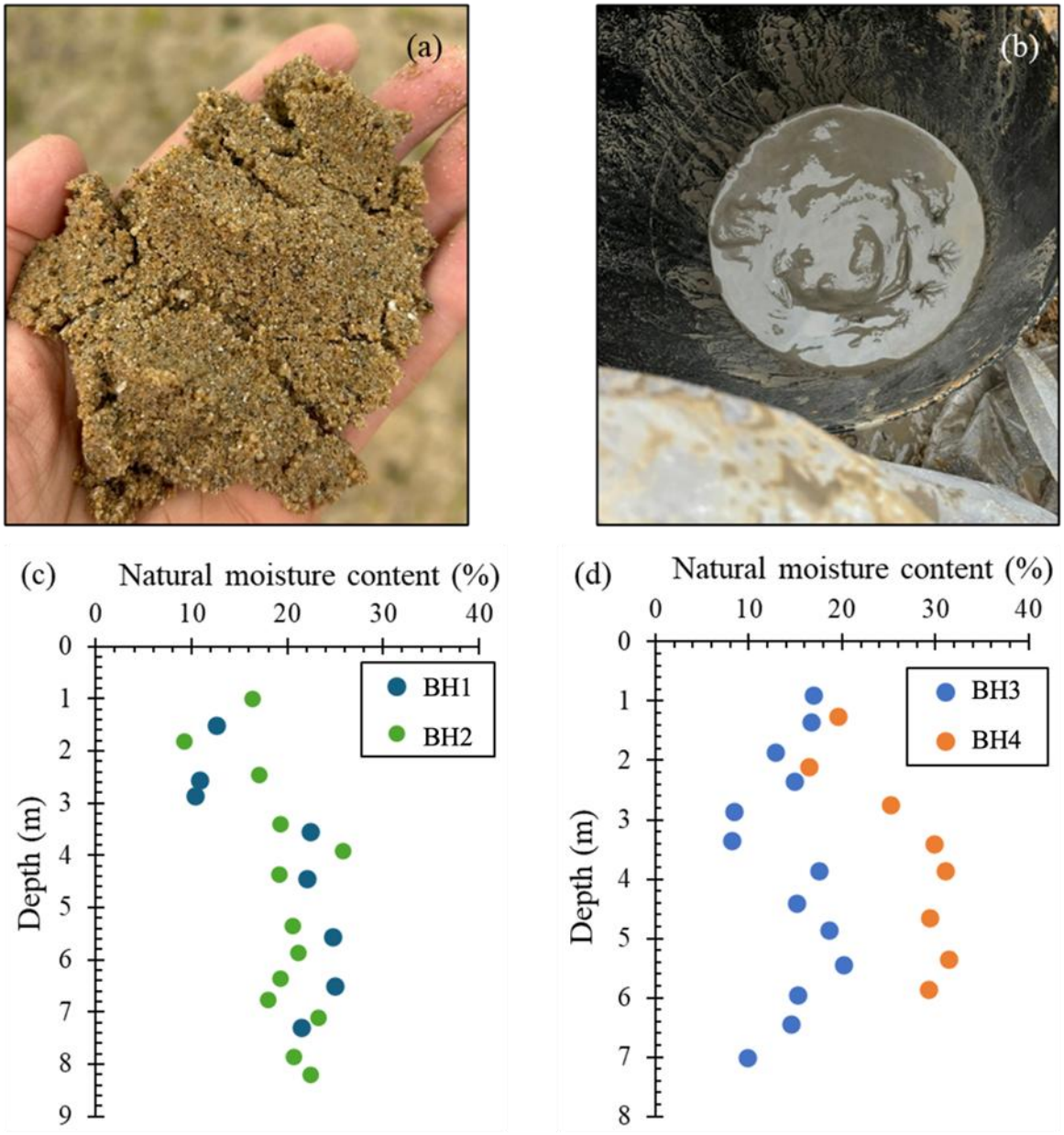

Figure 5. (a) Typical gravelly sand extracted from boreholes. (b) Dark grey fine silt observed in BH4. (c–d) Variation of natural moisture content with depth.

7. Chemical characterisation tests

Representative sand samples from the four boreholes were analysed with the wavelength-dispersive X-ray fluorescence (WD-XRF) and powdered X-ray diffraction (XRD) techniques to obtain the compositional and mineralogical information. As both techniques require powdered samples for

analysis, small quantities of oven-dried sand samples were crushed in a ball milling apparatus. The samples from four boreholes were separated into different groups for the chemical analyses, based on the visual description and grain size characteristics.

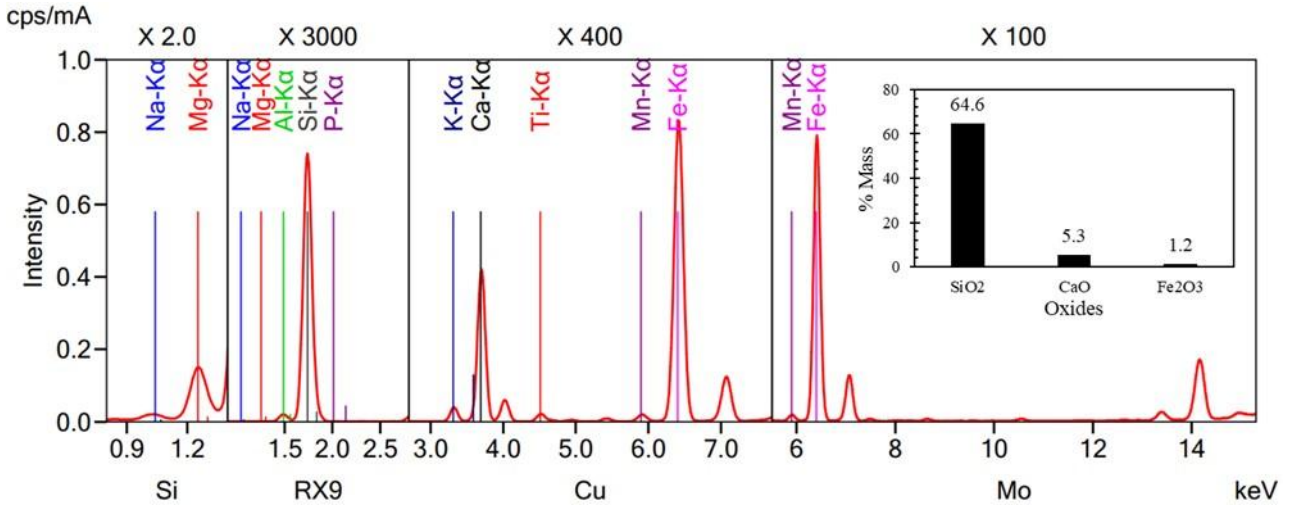

Figure 6. Element spectrum of the representative Kilmuckridge sand sample.

The WD-XRF intensity spectra of Kilmuckridge sand samples showed a dominant presence of silicon (Si), followed by calcium (Ca) and iron (Fe). Small traces of other elements such as sodium (Na), potassium (K), magnesium (Mg), and aluminium (Al) were found. A representative intensity spectrum of sand samples is shown in Figure 6. Energy dispersive ED-XRF also provides the percentage masses of primary elements present in the sample, and oxide analysis was carried out to estimate the mass percentages of oxides of those elements (based on balancing oxygen mass). The percentages of the dominant oxides from the four boreholes are shown in Table 3. High SiO_2 content dominates most samples (ranging from ~63% to 80%), confirming the quartz-rich nature of these soils. Al_2O_3 concentrations vary widely, with elevated values in layers with higher fines content, indicating a substantial presence of clay minerals, especially kaolinite and illite. MgO and Fe_2O_3 are moderately enriched in deeper samples, consistent with the presence of smectite and chlorite. Notably, K_2O and Na_2O concentrations align with the occurrence of feldspars and micas, while the consistent levels of CaO, often above 10%, may reflect minor calcite or plagioclase contributions [18,19]. These compositional trends can be supported by the mineralogical interpretations from XRD, reinforcing the complex interplay between detrital influx, weathering intensity, and post-depositional alteration.

Quantitative phase analysis of XRD spectra of the borehole samples was performed, and the results are shown in Table 4. Quartz is the dominant phase in many samples, reaching over 90% in some cases, which is indicative of a mature, stable source such as granitic or metamorphic rocks. Scanning electron microscopy (SEM) images showing angular to subrounded quartz grains support the interpretation of mechanical weathering and subsequent fluvioglacial transport. These quartz-rich units likely represent well-sorted, high-energy depositional environments, such as channel sands or reworked aeolian loess, which would retain minimal clay coatings or pedogenic alteration [18].

Table 3. WD-XRF quantitative analyses of elements (respective oxides) in borehole samples.

Element	BH1			BH2			BH3			BH4		
	B	E	G	B	E	M	C	E	K	B	D	G
	2.4 to 2.7 m	4.3 to 4.6 m	6.3 to 6.7 m	1.6 to 2.0 m	3.8 to 4.0 m	8.1 to 8.3 m	1.7 to 2.0 m	2.7 to 3.0 m	5.8 to 6.1 m	1.8 to 2.4 m	3.2 to 3.6 m	5.2 to 5.5 m
Na_2O	0.81	0.66	1.4	0.75	0.78	0.72	0.83	1.2	0.49	1.05	1.39	1.1
MgO	0.69	1.72	1.96	1.65	1.68	1.7	0.65	2.05	0.55	0.84	1.71	1.6
Al_2O_3	3.88	9.85	8.21	4.0	9.1	9.05	3.62	12.5	2.9	4.47	8.6	8.33
SiO_2	80.0	71.5	71.2	77.1	72.0	72.2	70.5	63.5	74.8	71.9	71.0	65.7
P_2O_5	0.11	0.18	0.18	0.15	0.14	0.16	0.11	0.23	0.11	0.13	0.19	0.19
K_2O	0.82	2.01	1.81	1.9	1.92	1.88	0.86	2.59	0.68	1.09	1.83	1.76
CaO	8.47	9.77	11.0	10.2	10.25	10.18	8.71	11.4	6.65	8.42	10.8	12.2
MnO	0.04	0.07	0.08	0.06	0.07	0.05	0.04	0.12	0.04	0.04	0.07	0.09
Fe_2O_3	1.74	3.45	3.2	3.1	3.15	3.12	1.42	5.24	1.23	1.18	2.43	3.2

In contrast, significant kaolinite concentrations are observed in several samples, most notably in BH2-E (58.3%) and BH1-E (46.9%), suggesting moderate to advanced chemical weathering under acidic, leaching conditions, consistent with temperate humid environments such as those found in southeast Ireland. The presence of pseudo-hexagonal platy kaolinite structures in SEM images further supports this interpretation. These zones may represent relict paleosols or altered horizons within a stratified sedimentary sequence, reflecting episodes of pedogenesis and subsequent burial. Their development is likely influenced by the underlying lithology, drainage regime, and regional climatic patterns favouring leaching and aluminium enrichment [20,21].

The presence of smectite and illite across different profiles suggests contributions from both in situ weathering and external detrital sources. Smectite, noted in BH1-G and BH4-G, typically forms under conditions of limited drainage and moderate base availability and may indicate localised diagenetic transformation or reworked volcaniclastics. Illite, identified in BH2-E and BH1-G, reflects lower degrees of chemical weathering and is commonly derived from the physical breakdown of mica-rich metamorphic rocks or partially altered feldspars [22]. Notably, the XRF-derived K_2O concentrations correlate with mica-bearing mineral phases, reinforcing the interpretation of illite and muscovite occurrence. The preservation of feldspars such as microcline, orthoclase, sanidine, and anorthoclase in multiple units further supports the hypothesis of either limited chemical weathering or relatively rapid sedimentation. These minerals are generally unstable under prolonged leaching but persist in soils where exposure to acidic percolation is limited or when encapsulated in coarser detrital fractions. SEM evidence of angular to blocky feldspar grains with minor surface etching supports a low degree of alteration, consistent with sediment profiles that experienced episodic deposition and brief subaerial exposure.

Table 4. XRD quantitative analyses of minerology in borehole samples.

Sample	Depth (m)		Visual description	Phase	Value ± ESD (%)
	From	To			
BH1-B	2.4	2.7	Gravelly sand	Quartz	76.4 ± 1.3
				Anorthoclase	9.9 ± 1.1
				Anorthite	9.8 ± 1.9
				Calcite	3.96 ± 0.3
BH1-E	4.3	4.6	Stiff sandy silt	Kaolinite	46.9 ± 1.4
				Quartz	39.8 ± 0.8
				Illite	5.6 ± 1.0
				Calcite	3.8 ± 0.2
				Muscovite	2.3 ± 0.6
				Chlorite	1.6 ± 0.3
BH1-G	6.3	6.7	Silty sand	Quartz	48.4 ± 1
				Smectite	23.6 ± 1.2
				Sanidine	10.9 ± 1.3
				Microcline	7.7 ± 1.2
				Calcite	6.3 ± 0.4
				Illite	3.07 ± 0.87
BH2-E	3.8	4.0	Stiff sandy silt	Kaolinite	58.3 ± 5.2
				Quartz	23.4 ± 2.9
				Illite	8.4 ± 1.4
				Calcite	4.5 ± 0.6
				Muscovite	3.4 ± 0.8
				Chlorite	2 ± 0.4
BH2-K	7.0	7.2	Silty sand	Quartz	88.7 ± 1
				Orthoclase	5.1 ± 0.8
				Muscovite	3.3 ± 0.8
				Calcite	2.91 ± 0.3
BH3-B	1.2	1.5	Slightly silty sand	Quartz	92.3 ± 1
				Microcline	7.7 ± 1
BH3-E	2.7	3.0	Silty sand	Quartz	49.6 ± 1
				Kaolinite	40.8 ± 1.6
				Microcline	4.97 ± 0.75
				Calcite	4.7 ± 0.3

Continued on next page

Sample	Depth (m)		Visual description	Phase	Value ± ESD (%)
	From	To			
BH3-F	3.2	3.5	Gravelly sand	Calcite	5 ± 0.4
				Quartz	85.6 ± 1.2
				Plagioclase	9.4 ± 1.2
BH3-M	6.8	7.2		Calcite	4.25 ± 0.3
				Anorthoclase	5.9 ± 0.6
				Muscovite	1.5 ± 0.4
				Quartz	54.6 ± 1.1
				Kaolinite	33.8 ± 1.6
BH4-B	1.8	2.4	Slightly gravelly sand	Calcite	3.69 ± 0.24
				Anorthoclase	6.73 ± 0.8
				Quartz	50.84 ± 0.71
				Kaolinite	34 ± 1.3
				Microcline	4.71 ± 0.5
BH4-D	3.2	3.6	Slightly sandy silt	Quartz	32.7 ± 0.6
				Calcite	4.26 ± 0.26
				Kaolinite	44.1 ± 1.8
				Microcline	5.79 ± 0.8
				Smectite	13.2 ± 1.1
BH4-G	5.2	5.5	Slightly sandy silt	Anorthoclase	8.06 ± 0.8
				Quartz	36.2 ± 0.6
				Kaolinite	34.2 ± 1.9
				Smectite	14 ± 1

Calcite, though minor (3%–6%), is consistently present and may have both detrital and diagenetic origins. It may reflect input from calcareous bedrock or biological sources, or it could be secondary, precipitated from groundwater under changing pH or CO_2 conditions. XRF results show higher CaO content in a few samples (e.g., BH2-E and BH4-G), which align with XRD detection of calcite and suggest at least partial diagenetic mobilisation and reprecipitation [19].

Overall, the mineralogical assemblages and their vertical distribution indicate alternating phases of sediment transport, pedogenesis, and diagenetic modification. BH3 largely reflects a transported, quartz-rich, mechanically sorted silt with minimal chemical transformation. In contrast, BH1 and BH2 contain kaolinite- and illite-enriched zones, pointing to prolonged chemical weathering and soil development. BH4 represents an intermediate case, where quartz dominance coexists with significant clay content, suggesting repeated cycles of sediment reworking, short-range transport, and post-depositional weathering. These findings are consistent with a dynamic depositional environment shaped by variable hydrological regimes, fluctuating base levels, and heterogeneity in sediment supply. The integration of mineralogical (XRD), elemental (XRF), and morphological (SEM) data provides a robust multi-proxy approach for reconstructing soil-forming processes and landscape evolution in temperate environments such as southeast Ireland.

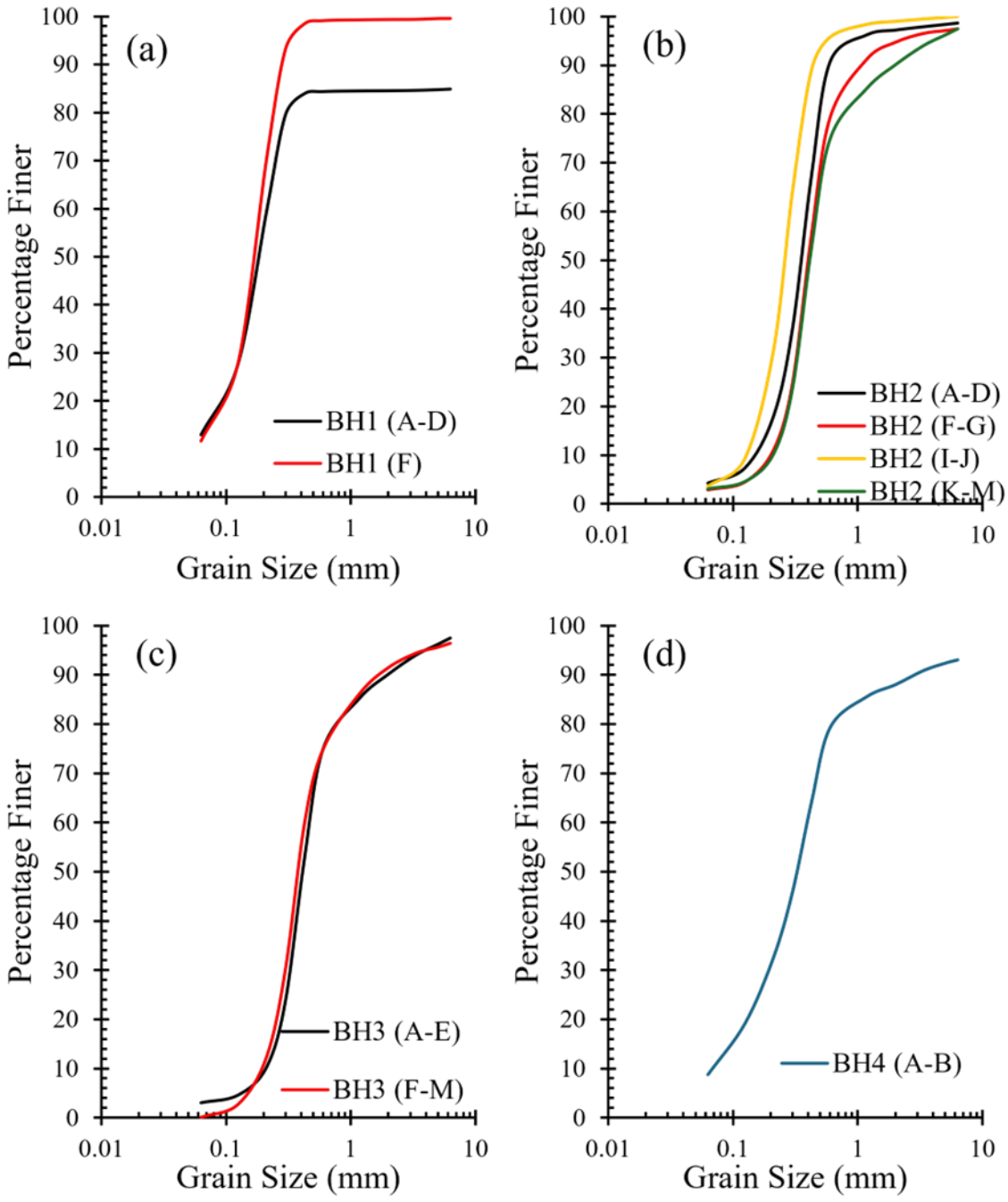

Figure 7. Representative particle size distribution curves of borehole samples (wet sieve).

8. Particle size distribution

The disturbed samples collected from the four boreholes were regrouped based on the visual observations, and particle size distribution sieve tests were performed. Wet sieve tests were performed on all the samples except for the silt extracted from BH1, BH2, and BH4 at specific depths (see Table 2). These silt samples have an average of 95% of the mass passing through a 63-μm sieve. Figure 7 shows the particle size distribution curves for the borehole samples collected from BH1 to BH4, which are dominantly gravelly sand to clean sand, with minor fractions finer than ~0.063 mm, indicating a

low fines content (maximum of 13% in BH1) and good drainage. Curves are generally steep, so most units are uniformly graded; however, some horizons include a measurable gravel fraction, most evident in BH1, while others are sand-dominant. Overall, the deposits are clean sands with gravel lenses in the top layers, supporting drained, frictional behaviour and limited sensitivity to plastic fines.

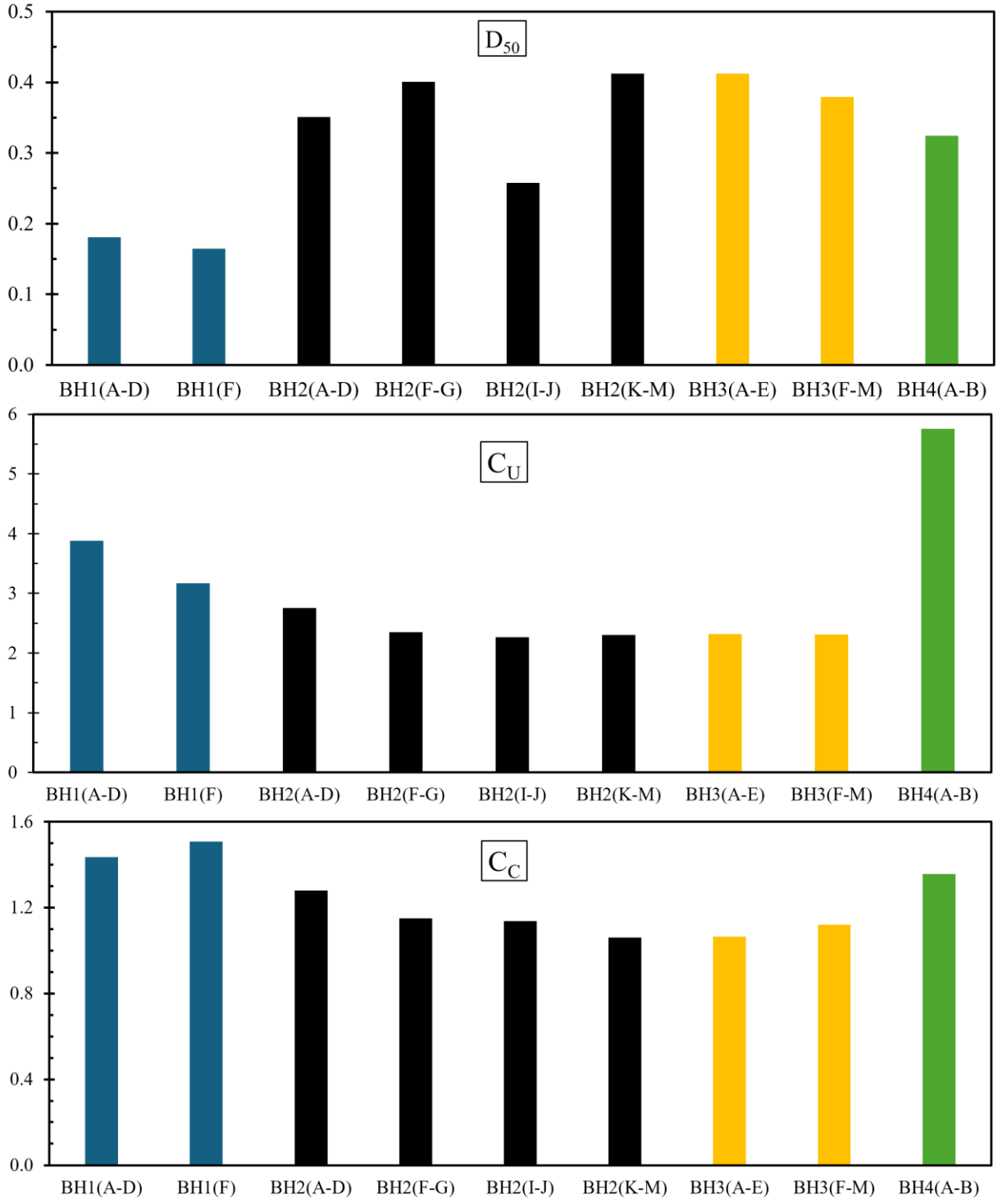

Figure 8. Variation of grain size characteristics with depth. (a) D_{50}, (b) uniformity coefficient, and (c) coefficient of curvature.

The grain size properties, such as D_{50}, uniformity coefficient (C_U, defined as D_{60}/D_{10}), and curvature coefficient (C_C, defined as $D_{30}^2/D_{10} \times D_{60}$) for these samples, are shown in Figure 8. These properties indicate that the borehole samples are mostly clean sands with modest spatial variability. D_{50} values span from 0.16 to 0.41 mm; BH1 is the finest (fine sand), BH2 and BH3 are predominantly medium sand, and BH4 is intermediate. Uniformity coefficients are mostly low with Cu values ranging between 2.1 and 3.8, suggesting a uniformly/poorly graded material; only BH4 with Cu of 5.8 suggests a well graded material. Curvature coefficients cluster around 1.1–1.5, suggesting smooth, single-mode gradations with no gap grading. Figure 9 shows the variation of fines (<0.063 mm), sand (0.063–2.0 mm), and gravel (>2.0 mm) contents (in percentage weights) with depth for the four boreholes. The thin, stiff silt layer observed in BH1 and BH2 (see Table 1) at about 4 m depth can also be observed in Figure 9, with a sharp increase in fines and a corresponding decrease in sand and gravel contents.

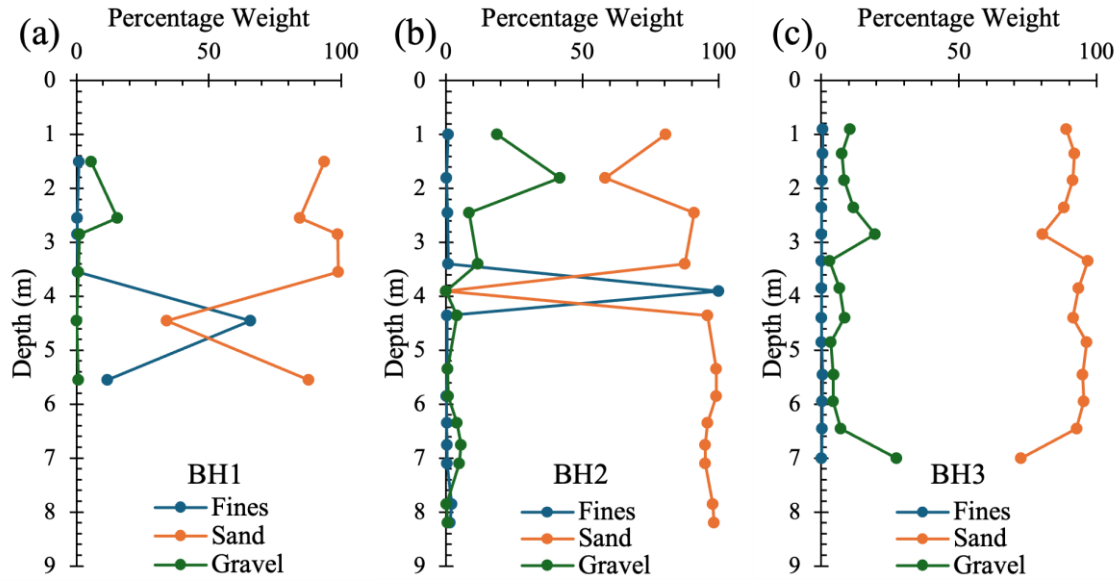

Figure 9. Variation of gravel, sand, and fine contents with depth in (a) BH1, (b) BH2, and (c) BH3.

9. Microscopic observations (grain shape and size)

High magnification images of representative samples from four boreholes were captured using a Zeiss GeminiSEM 460 field emission scanning electron microscope (FESEM) available at Trinity College Dublin, Advanced Microscopy Laboratory. A total of nine samples were selected for the images: three gravelly/silty sand samples from the top layers of BH1–BH3, three silty sand samples from the bottom layers of BH1–BH3, and three silt samples from BH1, BH2, and BH4. Figure 10 displays the nine images of these representative samples at different magnifications (500× and 4000×), highlighting various geometric and geological features of the samples.

Preliminary observation indicated that the gravelly sand and silty sand grains are subrounded to angular in shape, while the silt grains are highly angular. Predominantly, the geometrical features of the grains at higher magnifications (Figure 10c, d, and h) indicate that the deposits are a result of parent rock crushing, and the surface features include uneven (concave) fractures and earthy fractures

(crumbly in nature; Figure 10g). Many agglomerates of silt particles are present in the soil matrix (top right corner of Figure 10c), which break down into silt with finger pressure. The origin of such agglomerates of silt particles can be attributed to the cryoturbation shortly after glaciofluvial sedimentation [23]. In the soil matrix, the fine silt grains are strongly adhered to the sand and gravel particles despite blowing compressed air during SEM sample preparation, as these fine materials deposit into microfractures or pits on coarse grains during meltwater flow [24]. On the contrary, the sandy silt deposits in a thin layer at around 4 m depth in BH1 and BH2, and the fine silt material in BH4, represent rock flour with highly angular particles. Similar particle shapes and deposits were observed in Blessington, Ireland [7], about 50 km inland from the present test site. A combination of subglacial meltwater deposition and low flow energy (or shorter distance) can lead to preservation of angular shapes of silts [24,25].

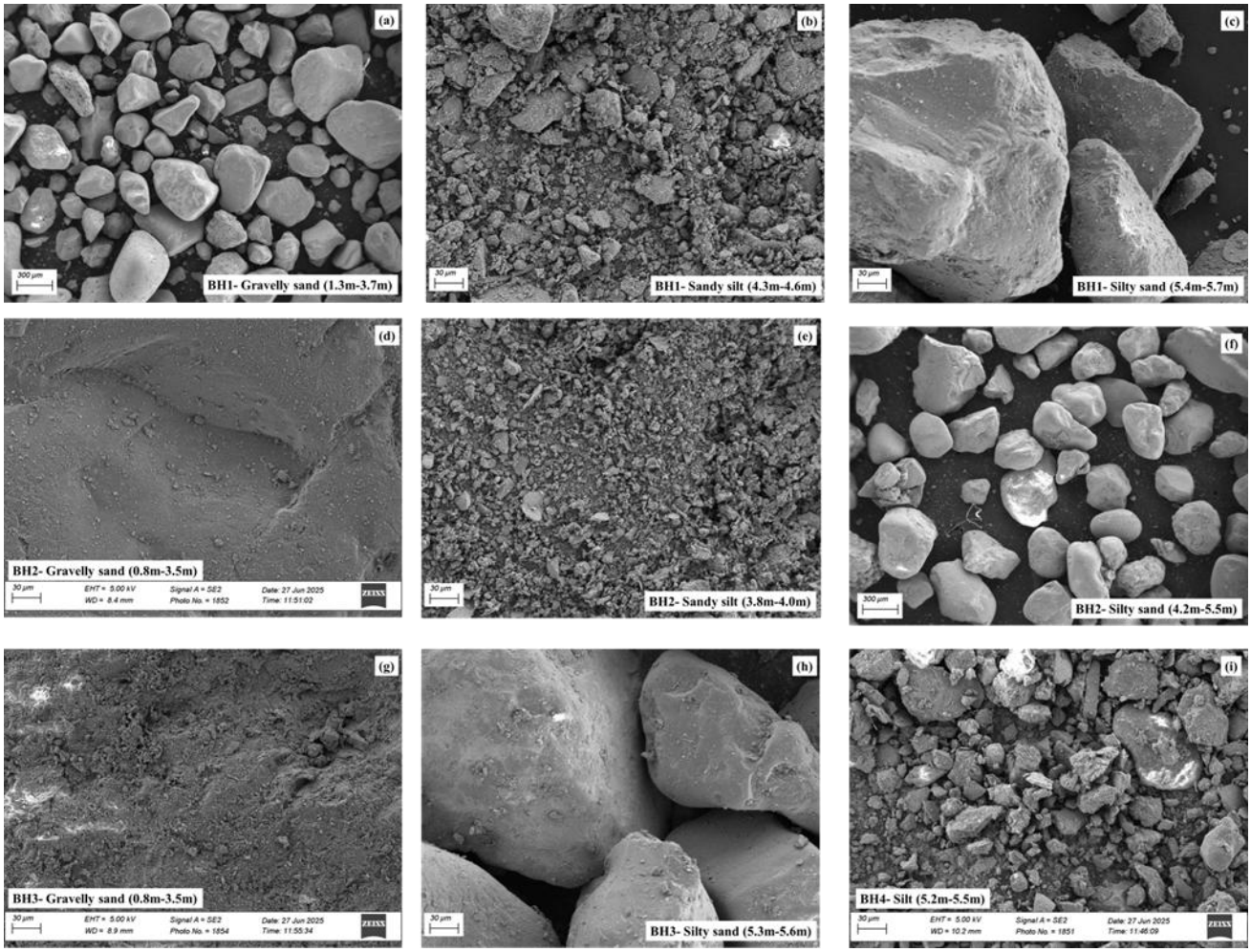

Figure 10. Representative scanning electron microscope images of borehole samples from Area A and Area B.

Quantification of 2D grain shape descriptors, circularity, and roundness for gravelly sand and silty sand particles was performed using ImageJ software to evaluate the grain shapes. Circularity is sensitive to boundary irregularities such as serrations and rough edges and is good for evaluating the

compactness and edge roughness of the particles (Eq. 1). On the other hand, roundness predominantly evaluates the elongation or aspect of the grains without regarding the boundary irregularities (Eq. 2).

$$Circularity = \frac{4\pi.Area}{(Perimeter)^2} \quad (1)$$

$$Roundness = \frac{4.Area}{\pi.(major\ axis\ length)^2} \quad (2)$$

The grain shape descriptor data obtained from the image analysis is separated into two groups: the top layers and bottom layers of a sedimentary sequence, based on the depths at which the samples were taken from the three boreholes (above and below the stiff silt band in BH1 and BH2). Figure 11 shows two binned 2D density plots that illustrate the relationship between circularity and roundness of grains from the top and bottom layers. In the bottom layers (Figure 11a), grain shapes are more widely distributed, with a significant proportion showing lower circularity and roundness values. This indicates the presence of less equant, more angular grains. The density is lower overall, with fewer high-frequency bins concentrated in the upper-right corner of the plot. In contrast, the top layers (Figure 11b) exhibit a more compact and sharply defined cluster of grains with both high circularity and high roundness, concentrated near the upper-right quadrant. This suggests a dominance of well-rounded, nearly circular grains in the upper stratigraphy. The consistent colour scale, where brighter colours represent higher counts per bin, confirms that the highest-density grain populations in the top layers are both rounder and more circular than those in the bottom layers. This shift in grain shape distribution likely reflects changes in sedimentary processes. The increased regularity and rounding of grains in the top layers may be attributed to longer transport distances, higher degrees of abrasion, or more selective reworking, resulting in more mature sediments. The bottom layers, with their broader spread and lower overall circularity and roundness, may represent less reworked or more proximal depositional conditions.

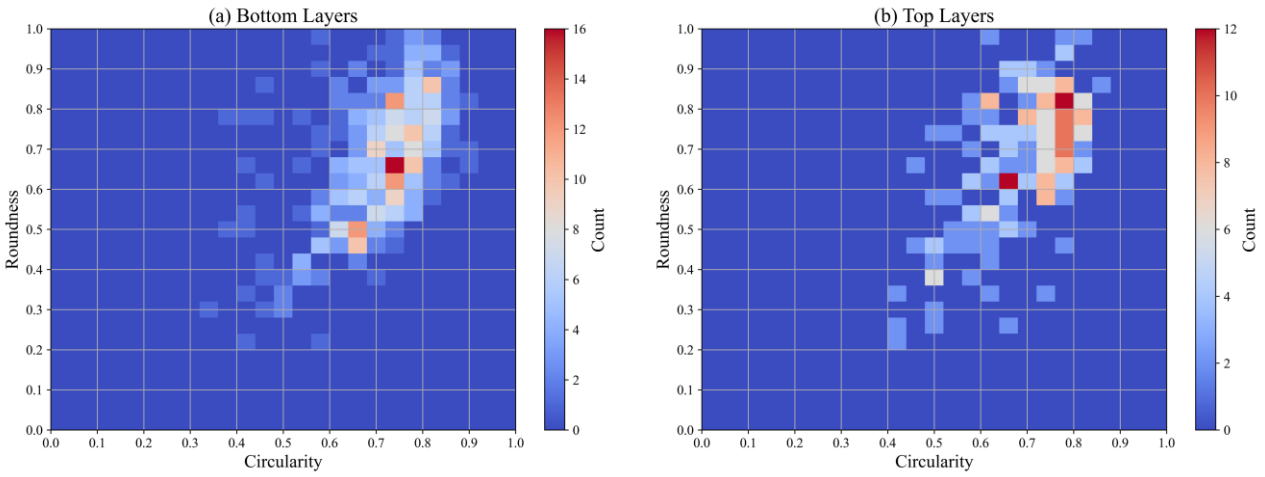

Figure 11. Comparison of 2D grain shape descriptors for particles from (a) bottom layers and (b) top layers.

Apart from the shape of the grains, there are significant differences in the sizes of the grains between the top and bottom layers. Figure 12 shows the violin plot visualising the grain area

distribution in the top and bottom sediment layers, highlighting key differences in size variability and central tendency. The top layer exhibits a broader distribution with a higher mean area ($\mu = 0.070$ mm², $\sigma = \pm 0.068$), suggesting the presence of larger and more heterogeneously sized grains. In contrast, the bottom layer shows a narrower, left-skewed distribution with a lower mean area ($\mu = 0.029$ mm², $\sigma = \pm 0.039$), indicating finer, more uniformly sized particles. This stratigraphic contrast may reflect shifting depositional energy conditions, where the top layer experienced either greater sediment supply or higher energy capable of transporting coarser grains. These variations in grain area align with earlier observations in circularity and roundness: grains in the top layer not only tend to be larger, but also more equant and rounded, consistent with increased transport distance or reworking. The bottom layer, with smaller and potentially more angular grains, may reflect a more proximal or low-energy depositional setting.

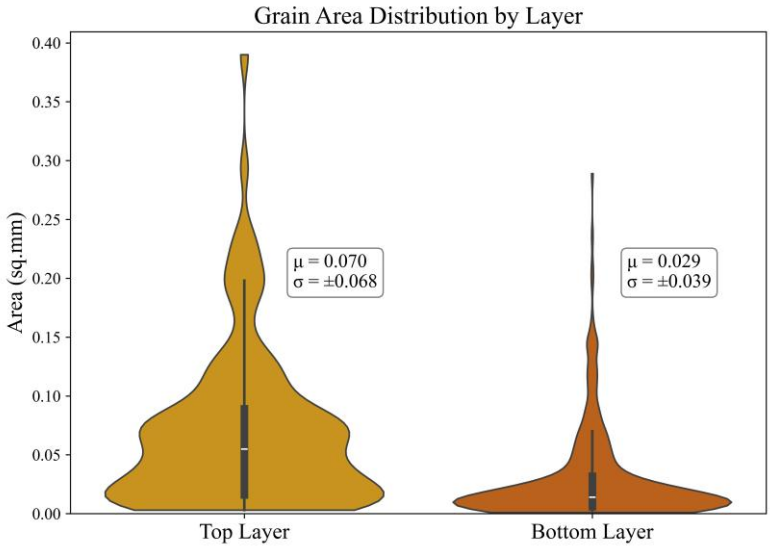

Figure 12. Comparison of distribution of grain areas of samples from the top and bottom layers.

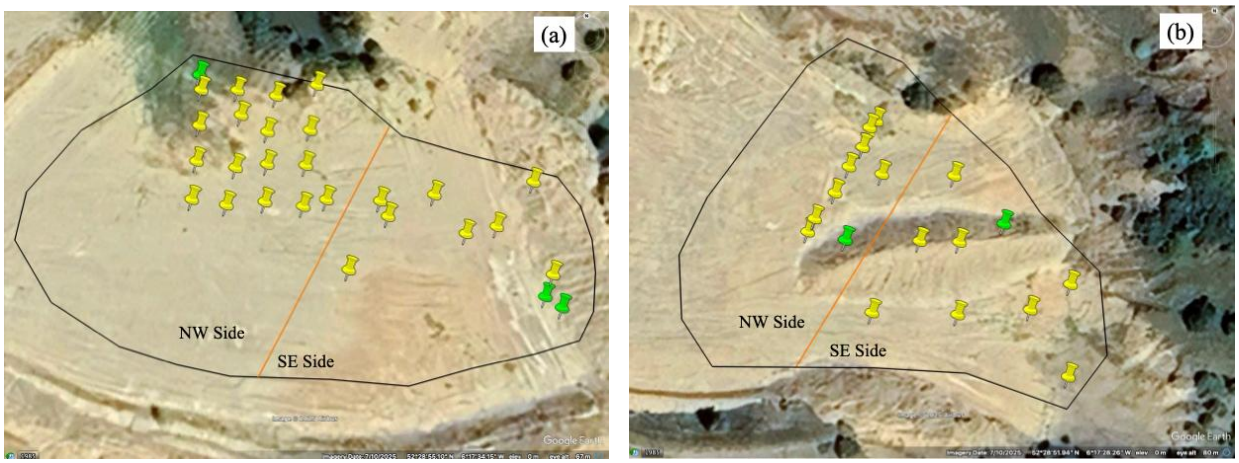

Figure 13. CPT test locations with separation of test groups in (a) Area A and (b) Area B.

10. CPT testing

A total of 25 CPTu tests and 3 SCPT tests were performed in Area A, and 16 CPTu tests and 2 SCPT tests in Area B. The CPT tests were performed to the depths of 10–12 m in the test site in accordance with the planned sizes of piles for lateral and axial load tests. Figure 13 shows the locations of the CPT tests in both areas (yellow pins indicate CPTu, and green pins indicate SCPT). The CPT profiles are grouped into four groups based on the test locations and the ground profiles observed: Area A (NW side), Area A (SE side), Area B (NW side), and Area B (SE side). The CPT profiles (cone resistance, sleeve friction, and pore water pressure) from Area A and Area B are shown in Figure 14 and Figure 15 respectively. The cone tip resistance (q_c), friction ratio (F_R), and pore water pressure measured behind the cone (u_2) are plotted. The patch plots show the range (minimum and maximum) values measured with depth, while the mean, 25th, and 75th percentile values are also plotted with depth.

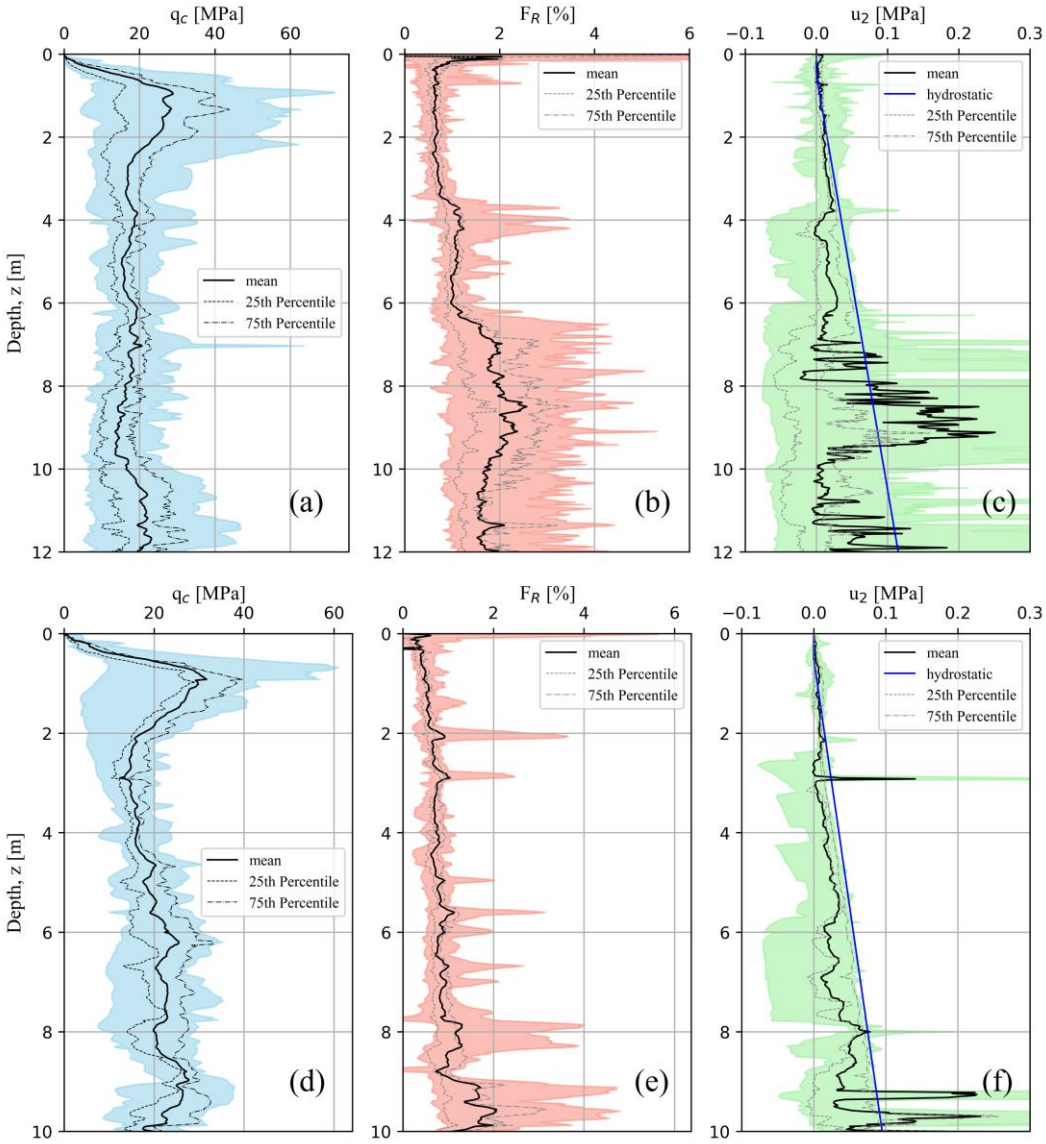

Figure 14. CPT profiles from 18 CPTs in Area A NW side (a–c), and 10 CPTs in Area A SE side (d–f).

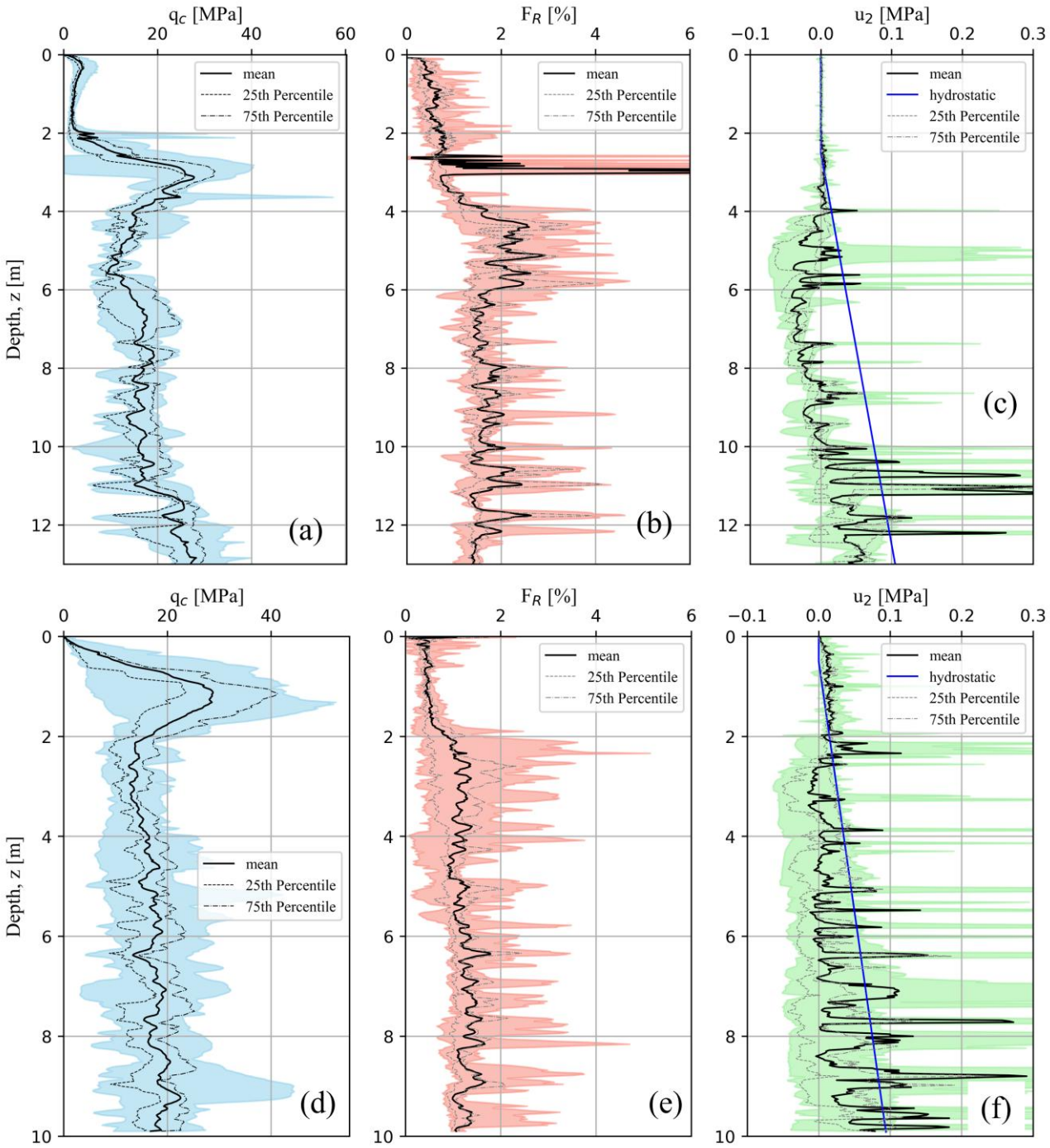

Figure 15. CPT profiles from 9 CPTs in Area B NW side (a–c), and 9 CPTs in Area B SE side (d–f) (see Figure 13 for locations).

In Area A (Figure 14a–f), the top layers of both test areas, up to around 2 m depth, show significant scatter with high cone resistances (q_c) up to 60 MPa. These high resistances are believed to be due to the presence of gravel and due to compaction as a result of heavy machinery tracking over this area. Below 2 m depth, the resistances drop to ~15–20 MPa. In the NW side of Area A (Figure 14a–c), a thin silt layer is observed at around 4 m depth, and, below the thin silt layer, a higher fines content is observed in BH1 (see Figure 9a). This is reflected in the drop in the u_2 profile from the hydrostatic line

below 4 m depth, along with a corresponding slight increase in friction ratio (F_R) between 4 and 6 m. Below 6.5 m depth, significantly higher F_R and positive u_2 values are observed in the NW side of Area A, indicating a higher fines content. In the SE side of Area A, a more consistent silty sand profile is seen at 8 m depth. It is observed that the mean u_2 values below 6.5 m are often higher than the 75th percentile, indicating the high positive values of u_2 are skewing the mean.

Area B is divided into two sides, with the SE (Figure 15j–l) consisting of ~2.5 m of natural silty sand underlain by slightly sandy silt (see BH4). The NW side of Area B (Figure 15g–i) has similar layering with the addition of 2 m of screened fill, which was placed on the natural ground prior to undertaking CPTs. Therefore, the elevation of the CPTs on the NW side is ~2 m higher than the SE side.

Two SCPT tests (SCPT3 and SCPT4 in NW and SE sides, respectively) were performed in Area A to investigate the variation of small-strain shear modulus (estimated from shear wave velocity, Vs) with depth. The seismic tests were performed at discrete depths of 0.5 m from 2 to 5 m depth and at every 1 m thereafter up to 14 m. The bulk density in Eq. 3 was calculated based on the empirical equation for unit weight (γ) from CPT parameters by [26] as shown in Eq. 4, assuming a particle specific gravity, $G_s = 2.65$.

$$G_0 = \rho V_s^2 \tag{3}$$

$$\frac{\gamma}{\gamma_w} = 0.27[\log F_r] + 0.36\left[\log\left(\frac{q_t}{p_a}\right)\right] + 1.236 \tag{4}$$

where F_r is the frictional ratio calculated as $(f_s/q_t) \times 100\%$, γ_w is the unit weight of water, and q_t is the cone resistance corrected for pore water pressure. The G_0 values measured from SCPT are compared with the estimates based on empirical correlations with cone resistance given by [27]:

$$G_0 = \alpha\left(q_c \cdot \sigma'_{v0} \cdot p_{ref}\right)^{0.33} \tag{5}$$

where the α value for uncemented sands is in the range of 110–280, and a value of 250 was used for this case, which gave a good fit with both SCPT test results (Figure 16a–b), with the exception of a few outlier points. The G_0 values estimated from shear wave velocities at location SCPT3 were about 150–200 MPa in the top 2 m gravel layer, below which consistent values occurred in the range 100–125 MPa. The SCPT4 location, approximately 50 m away from SCPT3, showed lower shear moduli at the shallow depths but increased significantly with depth. The small strain shear modulus trend for SCPT3 does provide a strong correlation (qualitatively) with the trend of cone tip resistances observed in Area A.

11. Multichannel analysis of surface waves (MASW) testing

1D and 2D MASW tests were performed in both test sites at five different locations. Emphasis was placed on understanding anisotropy in the test sites through shear modulus in transverse directions. The use of P- and S-wave measurements to identify anisotropy in geological materials is a common approach for rocks, particularly those influenced by the orientation of cracks in rock masses [28,29]. In this study, shear velocity profiles in two orthogonal directions were measured using MASW to note any differences in Vs and hence the small-strain shear modulus (G_0).

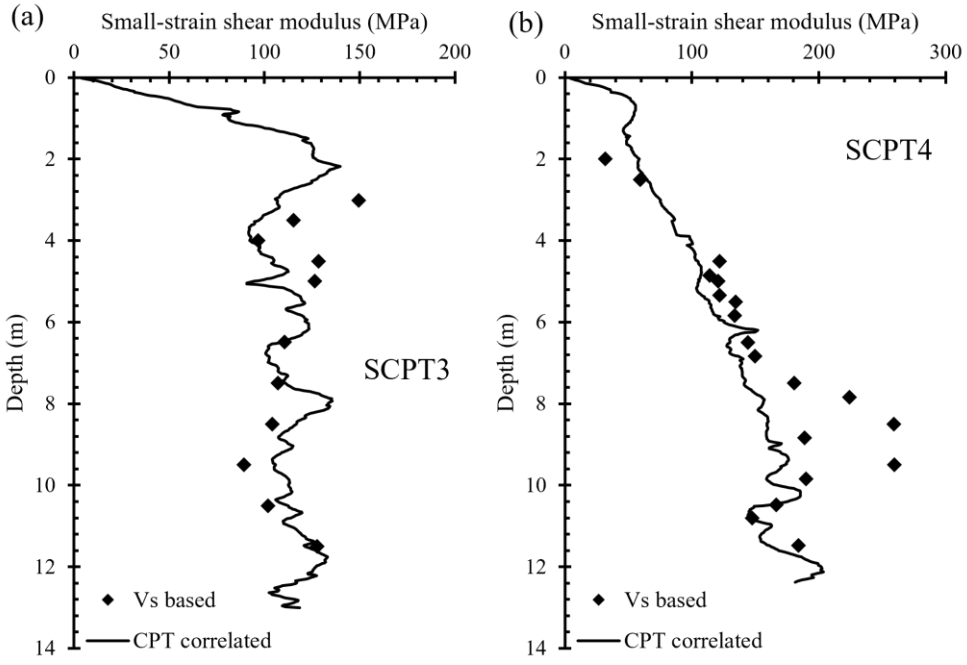

Figure 16. Comparison of G_0 from shear wave velocities and CPT correlations for two SCPTs.

Figure 17. Locations of MASW lines in two test areas.

1D active MASW tests were performed with the source placed 8 m away from the first of 24 geophones (10 Hz natural frequency) at 1 m spacing, resulting in the shear wave velocity measurement at the centre of the array. With the same centre location, the array of geophones is rotated 90° for the second test, resulting in shear wave velocities in orthogonal directions. One 2D MASW test in each of

the test sites was performed, with 1D profiles at every 2-m spacing for a total of 24 m. Figure 17 shows the lines of the MASW tests in both test sites.

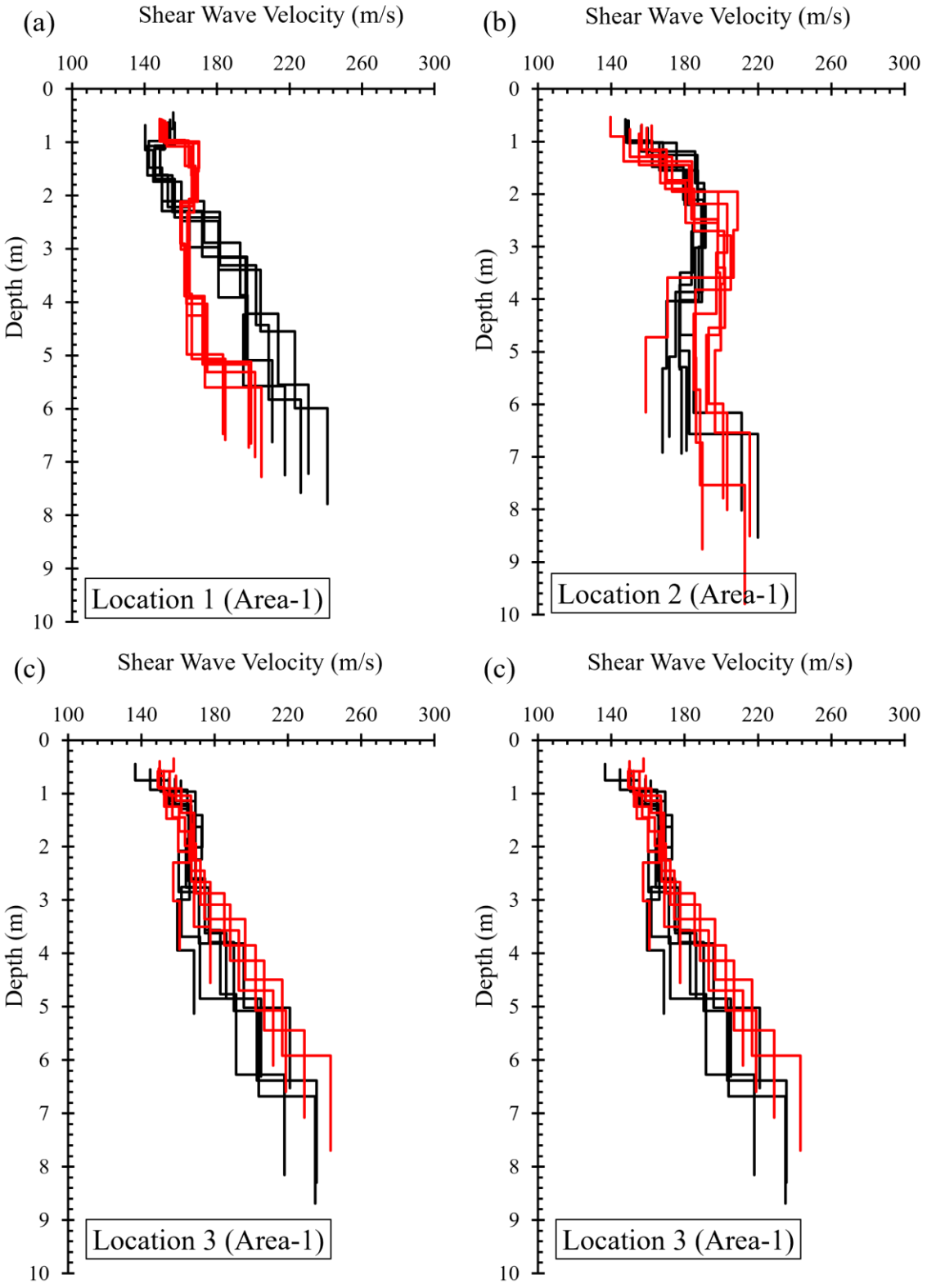

Figure 18. Shear wave velocity profiles in four locations across two test areas. Black and red lines indicate two transverse directions.

Figure 18a–d shows the shear wave velocity profiles captured at four different locations across two test areas (three locations in Area 1 and one location in Area 2, indicated in Figure 17). Across the four locations, the ground typically consists of three main layers. At all locations, a thin near-surface veneer shows low Vs (~140–170 m/s), consistent with made ground to about 1–3 m (gravelly sand). Below this, velocities rise into the ~170–210 m/s range, indicative of loose–medium granular soils, typically persisting to ~4–6 m. The basal portion generally attains ~210–250 m/s, characteristic of medium-dense to dense sand/gravel. Within Area 1, Location 2 presents the thickest soft cover (low V_s extending deeper before stiffening), Location 1 is intermediate with a modest mid-depth softening before recovery, and Location 3 shows the cleanest, steady increase in V_s with depth (location planned for pile load testing). Area 2 (Location 4) is comparatively stiffer, with the transition to ~210–250 m/s occurring shallower (around 4–5 m), suggesting that dense granular soils become predominant earlier. Overall, the profiles point to a soil sequence of loose near-surface materials over firm to stiff strata.

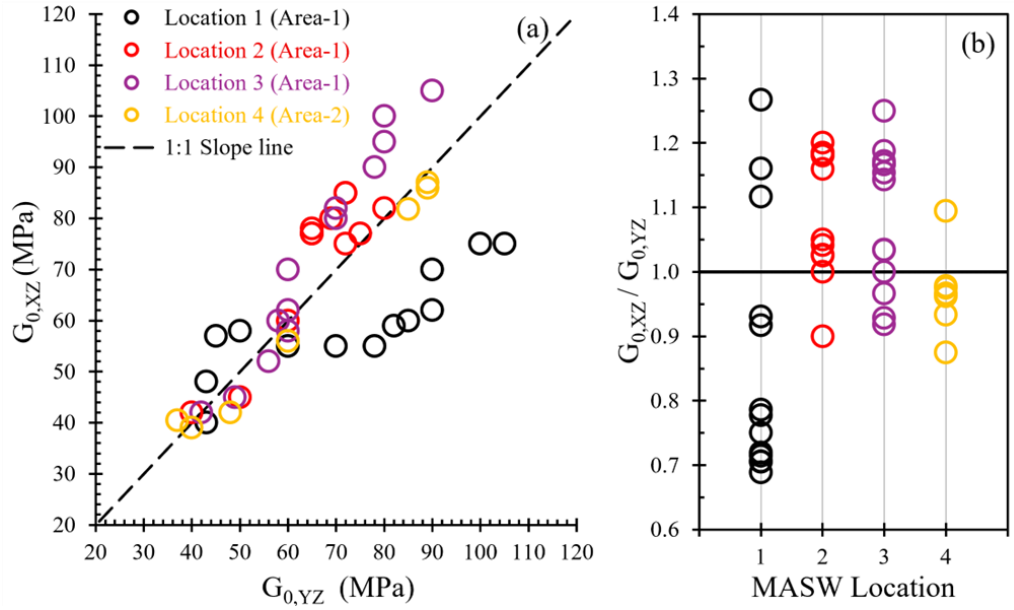

Figure 19. (a) Cross-plot comparing small-strain shear modulus in two transverse directions. (b) Shear modulus anisotropy ratio across four test locations.

The MASW results showed consistent layering but clear directional effects in both shear-wave velocity and small-strain stiffness. The red and black curves in Figure 18a–d represent the profiles measured in transverse directions at a given location. These profiles are represented in a cross-plot in Figure 19a, comparing $G_{0,XZ}$ with $G_{0,YZ}$ and demonstrating azimuthal anisotropy; points for Location 1 lie largely below the 45° line in deeper levels, those of Location 2 mainly above it, Location 3 clusters close to the line with modest scatter, and Location 4 showed the least anisotropy of all. Across the dataset, the calculated small-strain shear moduli span roughly 45–85 MPa, and the directional contrast typically ranges from 15% to 35%. This anisotropy is quantified as a ratio between the shear moduli in the two transverse directions ($G_{0,XZ}/G_{0,YZ}$), shown in Figure 19b. This pattern is not random noise but is systematic by orientation, indicating azimuthal stiffness linked to depositional fabric, preferred jointing, or stress-induced anisotropy.

The 2D MASW profile shown in Figure 20 indicates variable overburden thickness and stiffness; particularly, a sequence that begins with a soft veneer with Vs ranging between 140 and 170 m/s to around 2–3 m depth, overlying a layer that strengthens to 170–210 m/s by about 4–6 m, and a basal zone of 210–250 m/s representing medium-dense to dense sand. At the right end of the 2D line, roughly 10–15 m are governed by shallower, stiffer material; thus, a pile lateral loading response could give lower head deflections and reduced bending. Across the central part of the 2D MASW line, the thicker low-Vs cover could yield a more flexible response with larger lateral deflections and higher moments.

A comparison of small-strain shear modulus (G_0) values from SCPT and CPT correlations is shown in Figure 16. The Location 1 and Location 2 MASW tests, corresponding to M1–M2 and M3–M4 tests (see Figure 17), are relatively close to the AS03 and AS04 tests (see Figure 13). Overlying these MASW G_0 profiles on Figure 16 showed a reasonable comparison with the SCPT and CPT correlation-based values, as shown in Figure 21. However, the MASW profiles showed slightly lower shear modulus values than those of SCPT and CPT correlations. Unlike in SCPT, where point measurements are done, MASW performs a lateral and vertical averaging over the length of the geophone array. Given the complexity of vertical layering and high lateral heterogeneity in the Kilmuckridge test site, certain deviations between MASW and SCPT are expected.

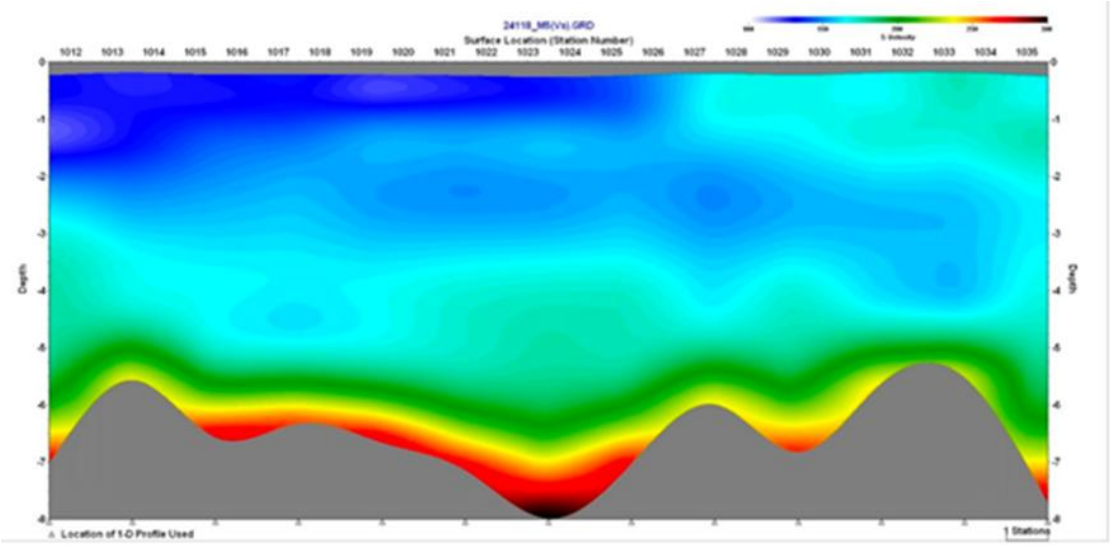

Figure 20. 2D MASW profile from Area A.

12. Shear strength tests (direct shear and triaxial testing)

Constant normal load (CNL) shear box tests (100 mm × 100 mm shear box) were performed on representative sand samples from the four boreholes across the two test areas. These tests were performed at 100% saturation level and relative density of 60%–75% in accordance with the field conditions (estimated based on CPT correlations) to estimate the shear strength of sand. These constant normal stress tests were performed at 25, 100, and 200 kPa. A representative set of shear stress and volume change curves (versus shear displacement) is shown in Figure 22.

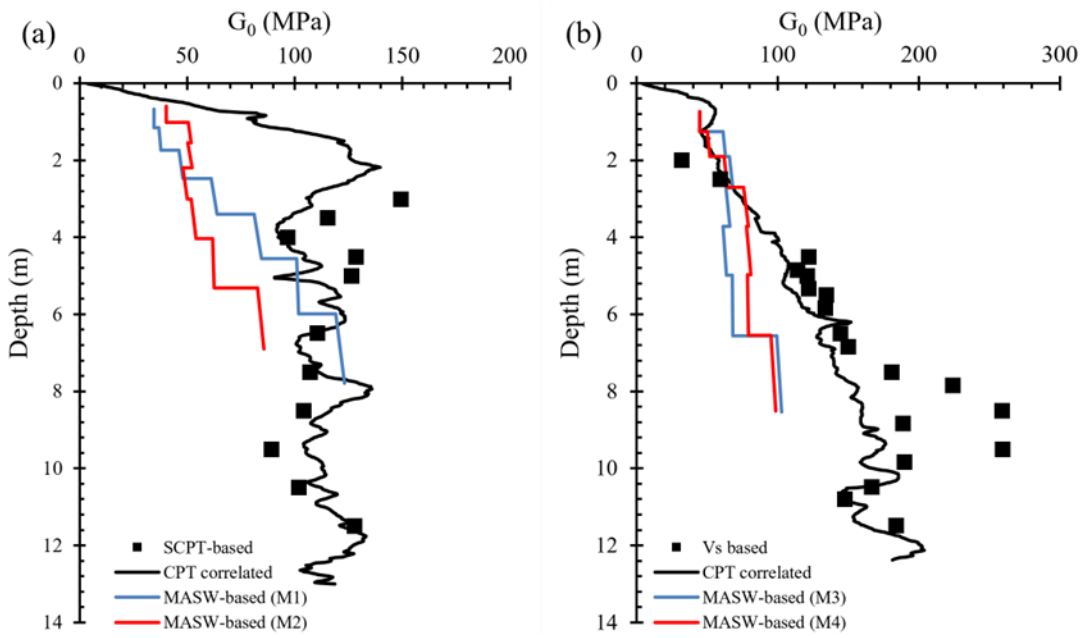

Figure 21. Comparison of G0 profiles based on SCPT, CPT correlations, and MASW at locations close to (a) Area A NW side and (b) Area A SE side.

The shear stress values are corrected for area change (reduction) as the shear displacement changed, and the volume change is calculated as the corrected area multiplied by the height of the sample at a given shear displacement. All the samples at three normal stresses showed a fully dilative behaviour with significant post-peak softening and an increase in the volume of the sample. The results from these tests are tabulated in Table 5. The peak friction angles range from 44.6° to 51.3° at 25 kPa and reduce systematically with increasing normal stress to 36.7°–41.2° at 200 kPa, showing strong stress-level dependence through dilatancy suppression. The volumetric behaviour shows a general trend of decreasing dilation with increasing normal stress, as expected for granular material.

In addition to the shear box tests, a representative set of monotonic drained triaxial tests was performed on the Kilmuckridge sand samples. The Kilmuckridge sand samples used for these triaxial tests are screened sand samples from the quarry site, where the screening was done in situ to remove any gravel greater than 6 mm in size. The geological origin of these screened sand samples is similar to that of borehole samples, with grain size distribution indicating poorly graded samples. The average values of D_{50}, C_U, and C_C of this sample are 0.39, 2.55, and 1.25, respectively, which closely resemble those of the silty sand sample (BH2 F-G; see Table 2) from the boreholes. A set of 6 monotonic drained triaxial tests were performed at different mean effective stresses (50–750 kPa) and two density states of 35% and 60% initial relative densities. Figure 23 shows the variation of mobilised friction angle and volumetric strain with axial strain during triaxial shearing. From these representative triaxial tests, the constant volume friction angle was observed to be around 32°–35°, with the peak friction angle depending on the mean effective stress, ranging from 35.1° at 750 kPa–35% Rd to 43.6° at 300 kPa–60% Rd. These friction angles are significantly lower than the value from shear box tests (albeit of slightly different grading) and could be attributed to slightly coarser content in the shear box test samples and the mode of shearing being different in these two tests.

One of the key inferences from both shear box and triaxial shear tests is that the Kilmuckridge sand is strongly dilative, significantly owing to the fact that the silty sand grains are dominantly rounded in shape (as observed from the SEM image analyses). The volumetric behaviours shown in Figure 22b for direct shear and Figure 23b for triaxial indicate a dilative behaviour.

Table 5. Summary of shear box tests on borehole sand samples.

Borehole	Sample code	Sample description	Normal stress (kPa)	Peak friction angle (°)	Maximum dilation (mm^3)
BH1	A–D	Slightly gravelly sand	25	45.3	6.38
			100	41.4	6.26
			200	41.2	3.92
	F	Slightly silty sand	25	47.8	7.59
			100	42.7	2.47
			200	40.7	2.52
BH2	A–D	Gravelly sand	25	50.2	6.34
			100	44.0	7.52
			200	36.7	5.80
	F–G	Gravelly sand	25	45.8	7.58
			100	43.2	6.34
			200	41.1	4.71
	I–J		25	50.6	7.76
			100	44.2	5.75
			200	42.8	4.83
	K–M	Silty sand	25	44.6	4.83
			100	43.3	3.67
			200	39.0	2.40
BH3	A–E	Slightly silty sand	25	51.3	7.26
			100	45.1	6.25
			200	40.7	4.26
	F–M	Gravelly sand	25	44.9	6.24
			100	41.1	5.45
			200	39.1	3.65
BH4	A–B	Slightly gravelly sand	25	50.8	7.96
			100	40.6	4.58
			200	40.0	3.72

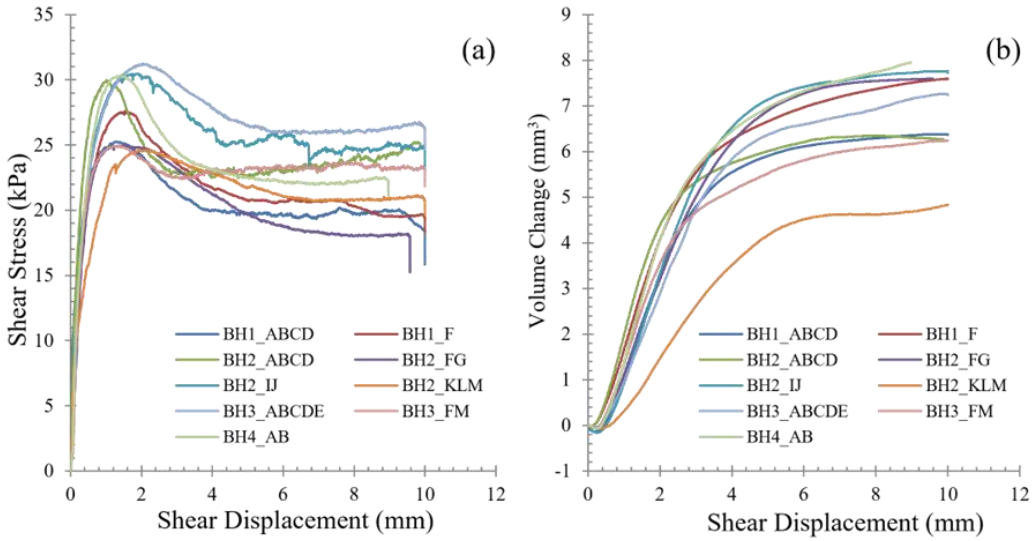

Figure 22. Representative results from shear box tests at 25 kPa constant normal stress. (a) Shear stress versus shear displacement. (b) Volume change versus shear displacement.

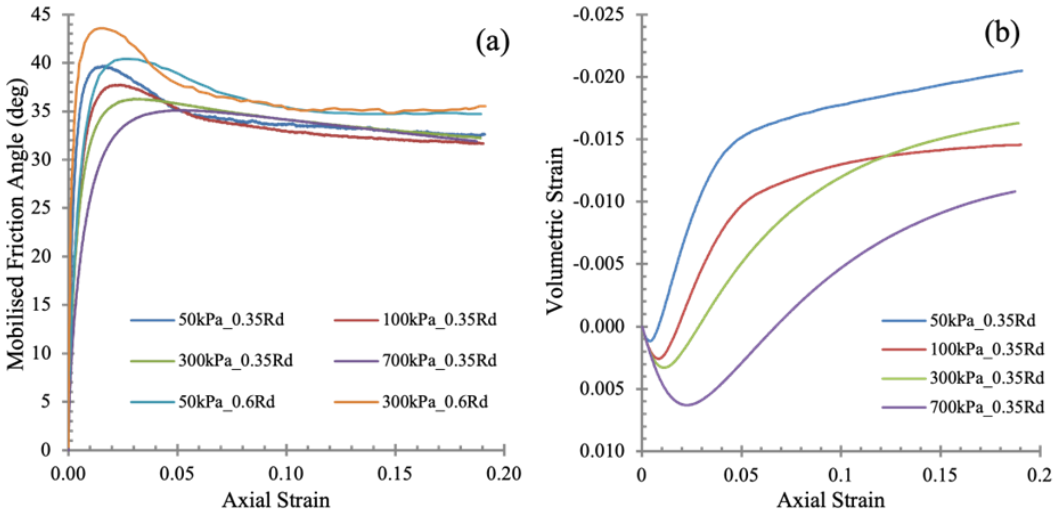

Figure 23. Monotonic drained triaxial test results on screened Kilmuckridge sand samples showing variation of (a) mobilised friction angle and (b) volumetric strain with axial strain.

13. Summary of site conditions

An overview of the geotechnical characterization of sand and silt test areas in the Kilmuckridge test site is provided in this paper. The strength and stiffness parameters measured from in situ and laboratory tests are summarised, and some empirical correlations relating the CPT test data to the stiffness parameter (G_0) are discussed. Some key insights from the reported work are:

1) The Kilmuckridge site exhibits lateral and vertical heterogeneity, with Area A dominated by slightly gravelly to silty sands and Area B by silty sand to sandy silt. CPT and borehole data confirm alternating layers of coarse and fine-grained material linked to glaciofluvial deposition.

2) Groundwater levels are shallow (0.6–1.6 m bgl) with measurable seasonal fluctuation correlated to rainfall. Hydraulic continuity between boreholes suggests limited vertical permeability despite the variability.
3) XRF and XRD analyses revealed quartz-rich (63%–80% SiO_2) sands with consistent calcite (3%–6%) and variable kaolinite, smectite, and illite; this indicates alternating mechanical and chemical weathering phases and episodic pedogenesis within temperate glacial–fluvial settings.
4) SEM observations demonstrate subrounded to angular quartz and feldspar grains with silt adhering to surface microfractures, implying cryoturbation and reworked glacial rock flour; quantified grain circularity and roundness confirm an upward fining and progressive textural maturity.
5) CPTu data reveal high cone resistances (up to 60 MPa) in the surface gravelly layers, dropping to 15–20 MPa in deeper sands, with friction ratios increasing at depths corresponding to silty horizons. These profiles indicate dense, over-consolidated sands with thin, low-permeability silt interbeds.
6) SCPT and MASW testing identified small-strain shear moduli (G_0) ranging 45–250 MPa, with 15%–35% azimuthal anisotropy attributed to depositional fabric and stress orientation; CPT-derived empirical correlations reliably reproduce measured G_0 trends.
7) Direct shear and triaxial tests confirm highly dilative, frictional response with peak friction angles 45°–51° at low stress, reducing to 37°–41° at 200 kPa due to dilatancy suppression. Constant volume friction angles of 32°–35° define drained strength for design calibration.
8) The comprehensive characterization confirms that the Kilmuckridge test site provides a representative over-consolidated test bed of sand and silt for advancing offshore foundation design methodologies. The site's stratigraphic complexity and anisotropic stiffness response will enable critical validation of computational models for predicting pile performance in comparable offshore deposits.

Author contributions

Sathwik Kasyap: Writing–original draft, Conceptualization, Investigation, Formal analysis, Visualization; Kevin Flynn: Writing–original draft, Investigation, Formal analysis; Mohammed Barzan: Data curation; Julie Labergere: Data curation; David Igoe: Conceptualization, Writing–review & editing, Investigation, Visualization, Supervision, Project Administration.

Use of AI tools declaration

The authors declare(s) they have not used Artificial Intelligence (AI) tools in the creation of this article.

Acknowledgments

The work described in this article was financially supported by Research Ireland (formerly Science Foundation Ireland) grant 21/EPSRC/3787 under the EPSRC-SFI Joint Research Grants Programme (EPSRC – Ref: EP/W006235/1), the Sustainable Energy Authority of Ireland (SEAI 23/RDD/1001), and Research Ireland (formerly Science Foundation Ireland) grant 22/FFP-P/11365.

Conflict of interest

The authors declare that there are no conflicts of interest with respect to the work reported in this article.

References

1. Byrne BW, McAdam RA, Burd HJ, et al. (2017) PISA: New design methods for offshore wind turbine monopiles. *Proceedings of the 8th International Conference on Offshore Site Investigation and Geotechnics*, Royal Geographical Society, London, UK, 142–161. https://doi.org/10.3723/OSIG17.142
2. Zdravkovic L, Jardine RJ, Taborda DMG, et al. (2020) Ground Characterisation for PISA pile testing and analysis. *Geotechnique* 70: 945–960. https://doi.org/10.1680/jgeot.18.PISA.001
3. Kallehave D, Byrne BW, LeBlanc-Thornton C, et al. (2012) Optimization of monopiles for offshore wind turbines. *Philos Trans A Math Phys Eng Sci* 373: 20140100. https://doi.org/10.1098/rsta.2014.0100
4. LeBlanc C, Houlsby GT, Byrne BW (2010). Response of stiff piles in sand to long-term cyclic lateral loading. *Géotechnique* 60: 79–90. https://doi.org/10.1680/geot.7.00196
5. Andersen KH (2009) Bearing capacity under cyclic loading—offshore, along the coast, and on land. *Can Geotech J* 46: 513–535. https://doi.org/10.1139/T09-003
6. Zhang JH, Zhang LM, Lu XB (2007) Centrifuge modeling of suction bucket foundations for platforms under ice-sheet-induced cyclic lateral loadings. *Ocean Eng* 34: 1069–1079. https://doi.org/10.1016/j.oceaneng.2006.08.009
7. Igoe D, Gavin K (2019) Characterization of the Blessington sand geotechnical test site. *AIMS Geosci* 5: 145–162. https://doi.org/10.3934/geosci.2019.2.145
8. Gavin K, Igoe D (2021) A field investigation into the mechanisms of pile ageing in sand. *Geotechnique* 71: 120–131. https://doi.org/10.1680/jgeot.18.P.235
9. Lapastoure LM, Igoe D (2024) Prediction of short piles response to lateral monotonic load in dense sand at Blessington, *Geotechnical Engineering Challenges to Meet Current and Emerging Needs of Society*, CRC Press, 3070–3073. https://doi.org/10.1201/9781003431749
10. Lunne T, Andersen KH, Low HE, et al. (2011) Guidelines for offshore in situ testing and interpretation in deepwater soft clays. *Can Geotech J* 48: 543–556. https://doi.org/10.1139/t10-088
11. Randolph MF, Low HE, Zhou H (2007) In Situ Testing For Design Of Pipeline And Anchoring Systems. *Proceedings of the 6th International Conference: Offshore Site Investigation—Confronting New Challenges and Sharing Knowledge*, Royal Geographical Society, London, UK, 251–262.
12. Williams JP, Aurora RP (1982) Case Study of an Integrated Geophysical and Geotechnical Site Investigation Program for a North Sea Platform. *14th Annual Offshore Technology Conference,* Houston, Texas. https://doi.org/10.4043/4168-MS
13. Creasey J, El Hajjar A, Conn AT, et al. (2025) ROBOCONE: PY module design development and calibration chamber testing in sand. *Proceedings of 5th International Symposium on Frontiers in Offshore Geotechnics*.

14. El Hajjar A, Creasey J, Conn AT, et al. (2025) Concept design and preliminary testing towards a new ROBOCONE tz module for in-situ cyclic soil characterization. *Proceedings of 5th International Symposium on Frontiers in Offshore Geotechnics*.
15. Tietzsch-Tyler D, Sleeman AG (1994) Geology of South Wexford. Geological Survey of Ireland.
16. Culleton EB (1978) Characterisation of Glacial Deposits in South Wexford. *Proc R Ir Acad Sect B* 78: 293–308. https://www.jstor.org/stable/20519062
17. Gardiner MJ, Ryan P (1966) Soil Survey Bulletin No. 1–Soils of Co. Wexford. National Soil Survey of Ireland, An Foras Taluntais.
18. Mitchell JK, Soga K (2005) *Fundamentals of soil behavior*, John Wiley & Sons Ltd., UK.
19. Rollinson HR (1993) *Using Geochemical Data: Evaluation, Presentation, Interpretation*, Routledge. https://doi.org/10.4324/9781315845548
20. Tardy Y (1997) *Petrology of laterites and tropical soils*, A.A. Balkema, Netherlands.
21. Singer MJ, Munns DN (2002) *Soils: An Introduction*, 6 Eds., Pearson, USA.
22. Chamley H (1989) *Clay Sedimentology*, 1 Ed., Springer Berlin, Germany. https://doi.org/10.1007/978-3-642-85916-8
23. Lepp AP, Miller LE, Anderson JB, et al. (2024) Insights into glacial processes from micromorphology of silt-sized sediment. *TC* 18: 2297–2319. https://doi.org/10.5194/tc-18-2297-2024
24. Crompton JW, Flowers GE, Dyck B (2020). Characterization of glacial silt and clay using automated mineralogy. *Ann Glaciol* 60: 49–65. https://doi.org/10.1017/aog.2019.45
25. Dreĭmanis A (1989) Tills: Their genetic terminology and classification, *Genetic classification of glacigenic deposits*, 17–83.
26. Robertson PK, Cabal K (2022) *Guide to cone penetration testing for geotechnical engineering*, 7 Eds.
27. Schnaid F, Lehane BM, Fahey M (2004) In situ test characterisation of unusual soils. *Second International Conference on Site Characterisation*, Millpress, Rotterdam, the Netherlands. 49–74.
28. Stan-Kłeczek I, Marciniak A (2023) Recognition of rock anisotropy using integrated seismic approach—A case in Strzegom and Podleśna, Poland. *J Rock Mech Geotech Eng* 15: 1759–1767. https://doi.org/10.1016/j.jrmge.2023.03.005
29. Colombero C, Comina C, Umili G. et al. (2016) Multiscale geophysical characterization of an unstable rock mass. *Tectonophysics* 675: 275–289. https://doi.org/10.1016/j.tecto.2016.02.045